공학박사 학위논문

Study on improvements of near-eye holography: form factor, field of view, and speckle noise reduction

근안 홀로그래픽 디스플레이의 개선에 관한 연구: 폼 팩터, 시야 각, 스페클 노이즈

2018년 2월

서울대학교 대학원

전기·컴퓨터공학부

리 강

Abstract

Study on improvements of near-eye holography: form factor, field of view, and speckle noise reduction

Gang Li

Department of Electrical Engineering and Computer Science

College of Engineering

Seoul National University

This dissertation presents solutions targeting on the three fundamental issues on near-eye holography: 1. Form factor, 2. Field of view (FOV), and 3. Speckle noise.

For the form factor reduction of the holographic display, a multifunctional holographic optical element (HOE) is developed to replace the beam splitter and the eyepiece lens of the conventional holographic display. As a result, it enables us to build a compact see-through holographic display for augmented reality (AR). The feasibility of using HOE in the holographic display is verified by analyzing some optical characteristics of the HOE, based on the Kogelnik's coupled-wave theory. In addition, a compensation method is introduced to compensate the wavefront aberration caused by use of the HOE.

To build a wide FOV holographic head mounted display, I proposed two methods to increase the space bandwidth product (SBP) which can widen the

FOV without losing eyebox size. In each optical path of $+1^{st}$, 0^{th}, -1^{st} diffraction order of a spatial light modulator (SLM), I place a shutter synchronized with the SLM to display different holograms by temporally dividing the frames of the SLM. The second proposed method is called *polarization selective holography* which is a brand new hologram calculation and encoding method. In this work, an SLM can modulate waves in different modes through different states of wave retardation and polarization optical elements. Two sets of wave plates and polarizers with optimized states are placed in the path of $+1^{st}$ and -1^{st} different diffraction orders of an SLM, so that the SLM reconstructs two different holograms via each path. As a result, the system achieves a two-fold increase in terms of SBP for a single SLM. Furthermore, a curved hologram can provide wider FOV comparing to a planar one, when they have the same SBP. A curved surface hologram can provide wider FOV. Thus, curved holographic display has a great potential to the near-eye holography. Since the curved surface SLM has not been developed yet, as an example, I also proposed a numerical method of spherical hologram computation of real objects in this chapter.

For the speckle noise issue, some analyses are carried out to compare the quality of holographic reconstruction images using different light source such as a light-emitting diode (LED) and a laser diode (LD). Both of them have pros and cons. The main advantage of use of the LED in the holographic display is it can reconstruct the holographic image with significantly less speckle noise compared to laser or LD. However, an inherent problem caused by use of the LED is that it is difficult to reconstruct images located far away from the SLM. This problem is mitigated using a magnifier optical system. As

a result, I demonstrate an LED based near-eye holographic display system not only to reduce the speckle noise but also to provide sufficient expressible depth range.

Keywords: Holographic display, augmented reality, virtual reality, form factor, holographic optical element, field of view, space bandwidth product, high-order diffraction, wavefront aberration, speckle noise, coherency

Student Number: 2013-31297

Contents

Abstract ..... **i**

Contents ..... **iv**

List of Tables ..... **vii**

List of Figures ..... **viii**

Chapter 1 Introduction **1**

1.1 Overview of near-eye displays 1

1.2 Motivation of this dissertation 7

1.3 Scope and organization 9

Chapter 2 Form factor reduction of near-eye holography using a multifunctional holographic optical element **11**

2.1 Introduction of form factor issues in near-eye holographic display 11

2.2 Introduction of volume hologram 13

2.2.1 Diffraction efficiency: Coupled-wave theory 14

2.2.2 Condition to be met for using holographic optical element in holographic display 19

2.3 Multifunctional holographic optcal element fabrication and application 27

2.3.1 Design of mirror-lens holographic optical element 27

2.3.2 Fabrication of mirror-lens holographic optical element 30

2.3.3 System implementation and experimental results 33

2.4 Wavefront aberration compensation method for holographic optical element 37

2.5 Summary and discussion 44

Chapter 3 Field of view expansion of near-eye holographic display **45**

3.1 Overview of field of view expansion for near-eyeholography 45

3.1.1 Investigation on constrains in expanding field of view for near-eye holography 45

3.1.2 Previous space bandwidth product enhancement methods for holographic display 50
3.2 Temporal multiplexing of high-order diffraction guided by holographic attenuating mirror 53
3.2.1 Design of holographic attenuating mirror 54
3.2.2 System imprelentation and expperiment results 60
3.3 Polarization selective holography 67
3.3.1 Principle of polarization selective holography 67
3.3.2 Amplitude combination map optimization using genetic algorithm 71
3.3.3 Simulation and experimental results 73
3.4 Synthesis of computer generated spherical hologram 76
3.4.1 Spatial spectral bandwidth of spherical hologram 76
3.4.2 Spherical hologram calculation of real objects 81
3.4.3 Simulation and experimental results 88
3.5 Summary and discussion 95
Chapter 4 Light source selection for near-eye holography 97
4.1 Coherence of light source 97
4.1.1 Temporal coherence 97
4.1.2 Spatial coherence 98
4.2 Image sharpness for holographic display 101
4.3 Ideal optical design for LED based near-eye holography 105
4.4 Summary and discussion 108
Chapter 5 Conclusion 109
Bibliography 111
Appendix 121

List of Tables

Table 1.1 Features of expressible depth range for 3D displays. 6
Table 2.1 Zernike polynomial coefficients of compensation. 42
Table 3.1 Definition of the FOV and eyebox size in the two types of near-eye holography. 47
Table 3.2 Parameters of the relay lenses and virture SLMs. 65
Table 4.1 Features of the two light sources (same spatial coherence) for holographic display. 105

List of Figures

Figure 1.1 Features of Human visual perception in accordance with FOV 3
Figure 1.2 The objective and the scope of the dissertation 10
Figure 2.1 (a) Optical configuration of conventional holographci display. (b) Concept of the multifunctional HOE..... 11
Figure 2.2 Diffraction in a volume grating..... 13
Figure 2.3 Model of diffraction in a volume grating..... 15
Figure 2.4 Diffraction efficiency distribution (Bragg-matched condition) according to the different angles of reference and signal waves. (a) Transmission grating and (b) reflection grating. 20
Figure 2.5 Angular selectivity of (a) reflection grating and (b) transmission grating. 22
Figure 2.6 Experiment setup for validate the feasibility of HOE for hologrpahic display 23
Figure 2.7 Experiment and simulation results for validate the feasiblity of HOE for holographic display. (a) Angular deviation of reconstructed wave and (b) diffraction efficiency according to the angular deviation of probe wave. 24
Figure 2.8 Resloving power comparison between a normal lens and a HOE lens. 25
Figure 2.9 Aberration comparison between a normal lens and a HOE lens.... 26
Figure 2.10 Schematic diagram of the MLHOE recording and reconstruction procedures. 28
Figure 2.11 Experiment to investigate aberrations of HOE lens the hologram reconstruction procedure. 29
Figure 2.12 Diffraction efficiency distribution according to exposure energies. 31

Figure 2.13 Experiment setup for (a) 1st step and (b) 2nd step of the MLHOE recording process..... 33
Figure 2.14 Protopype of the compact holographic display using MLHOE… 34
Figure 2.15 Experimental results: camera focus at (a) the Fourier plane of the SLM, (b) the MLHOE, and (c) the real object “Rubik’s cube,” (d) Camera is set to have a large depth of focus. 35
Figure 2.16 Experimental setup. 39
Figure 2.17 (a) Extracted phase of LHOE (b) Zernike polynomials (c) Zernike polynomials of aberration term. 41
Figure 2.18 Zernike polynomials of correction wavefront (b) phase of wavefront (c) converted gray-scale image. 41
Figure 2.19 PSF images (a) before compensation on Bragg matching (b) after compensation on Bragg matching (c) before compensation on Bragg mismatching (d) after compensation on Bragg mismatching 42
Figure 3.1 Optical designs for near-eye holography. 46
Figure 3.2 Experiment schematic diagram and setup of a wide FOV near-eye holographic display. 47
Figure 3.3 Experimental results: (a) reconstructed image when the camera focuses at 5 diopter. (b) Reconstructed image when the camera focuses at 0 diopter. 48
Figure 3.4 FOV and DOF variation according to eyebox size in a holographic display (SLM pixel number 1920×1080, pixel pitch: 8 um) 49
Figure 3.5 Schematic diagram of proposed method. 53
Figure 3.6 Grating detuning effect caused by dimensional shrinkage. 54
Figure 3.7 Vector space diagram for original grating and detuned grating cases. 55
Figure 3.8 Schematic of the (a) recording and (b) reconstruction processes .. 57
Figure 3.9 Diffraction efficiency according to exposure energy. 60

Figure 3.10 Guided three diffraction orders by the HOEs. 61
Figure 3.11 Measurement of FZP aberration. (a) Configuration and (b) experimental setup. (c) Captured reconstruction images 62
Figure 3.12 Comparisons of the reconstructed holograms: (a) without using the compensation method and (b) using the compensation method. 63
Figure 3.13 Configuration of proposed holographic display system. 64
Figure 3.14 Experiment setup of the proposed holographic display system... 65
Figure 3.15 Experimental results of the reconstructed holograms by the holographic display with increased SBP. 66
Figure 3.16 Concept of the polarization selective holography. 67
Figure 3.17 Ideal case of ACM for an 8 bit gray level SLM. 69
Figure 3.18 Single-sideband encoding method for amplitude-only SLM. 70
Figure 3.19 Flow chart of the genetic algorithm. 72
Figure 3.20 ACM and HCM distribution at A_1-A_2 plane. 73
Figure 3.21 Simulation results using polarization selective holography. 74
Figure 3.22 (a) Experiment setup. Reconstruction images: (b) -1st diffraction mode, (c) +1st diffraction mode. 75
Figure 3.23 (a) Position of the object point and the hologram surface. (b) Amplitude and (c) phase distribution of the spherical hologram. . 77
Figure 3.24 Object points with the same distance from coordinate origin..... 79
Figure 3.25 Spherical and planar hologram for optical field of the same FOV…..... 80
Figure 3.26 Required number of samples for the spherical and the planar hologram. d'= 0.18 m, r=1 m 81
Figure 3.27 Extracted depth maps of the object in multiple directions. (a) Colr images of the object, (b) corresponding depth map images. 82
Figure 3.28 Rotation of the initial point cloud sets. (a) Initial point clouds and (b) rotated ones..... 83

Figure 3.29 Acquired 3D model of the real object. 85
Figure 3.30 Speherical flipping of the 3D point cloud by Eq. (3.24). The object point cloud $\hat{P}_T$ and the flipped point cloud $\hat{P}_f$ 86
Figure 3.31 (a) Entire points without HPR and (b) the visible point set processed by HPR at the hologram point H_r(90°, 90°).. 87
Figure 3.32 Visible point set for each hologram point.. 87
Figure 3.33 Spherical hologram generated by one point object. (a) Amplitude and (b) phase images. 89
Figure 3.34 Amplitude of the generated spherical hologram. 90
Figure 3.35 Reconstruction process of the selected region. 91
Figure 3.36 Reconstruction of the partial regions of the spherical hologram. (a) Amplitude, (b) phase and (c) reconstruction image of the selected hologram region. 93
Figure 3.37 (a) Reconstruction image from a partial region of the proposed spherical hologram, (b) reconstruction image from the spherical hologram generated without using the HPR algorithm.. 94
Figure 4.1 Correlation between two light points from a light source..... 99
Figure 4.2 Comparison of image sharpness using light sources with different coherencies. (a) How temporal coherencce and (b) spatial coherence affect qualty of reconstruction images. 102
Figure 4.3 (a) Holograms reconstructed at different depths from an SLM using LD and LED light source. (b) Spectrum of the light source. 104
Figure 4.4 Optical design for the near-eye holography using a light source with low temporal coherence.. 106
Figure 4.5 Reconstructed hologram at different depth plane using the proposed optical configuraation. 107

Chapter 1 Introduction

1.1 Overview of near-eye displays

Since virtual reality (VR) and augmented reality (AR) have widely gained spotlights, the near-eye display has recently become an attractive research field. The near-eye displays have great potentials in various fields such as education, teleconferencing, scientific visualization, entertainment, military, and training [1]. So far, plenty of studies have been introduced in the both academia and industry area. Recently, the launch of several commercialized near-eye displays such as Oculus Rift, HTC VIVE, PlayStation VR, Samsung Gear VR, Google Glass, and HoloLens, open the new era where people can cross the real and the virtual world. However, those commercialized products still have many problems. Some main issues for realizing an ideal VR/AR device are as follows:

Form factor: One main reason that causes large and heavyweight form factor is the embedded various optical elements. A head-mounted display (HMD) requires magnifier optics and beam guiding optics. To provide a sufficient field of view (FOV) the diameter of an eyepiece lens should be large enough. So far, researchers have proposed many alternative ways to replace the conventional heavyweight and large size imaging optics in the HMD system. Currently, a popular schematic for getting a good form factor of the AR/VR devices is the waveguide (or lightguide) combined with a set of coupling gratings (in-coupling & out-coupling) [3-7]. The in-coupling

grating could be diffractive optical element (DOE) or holographic optical element (HOE). The coupled light propagates through the waveguide (or lightguide) via total internal reflection and it is out-coupled when it hits the out-coupling grating. As a result, the use of DOE and HOE enables us to reduce the form factor.

FOV: To provide an immersive experience, the HMD should provide a sufficient large FOV. Figure 1.1 describes the features of human visual perception in accordance with the FOV. As shown in Fig. 1.1, different FOV range is used to perceive different properties of image. The foveal vision zone, which has 3°-5° FOV, is the part of the retina that permits maximum visual acuity [2]. In general, the eye rotation left and right from one's normal line of sight is 15 degrees, thus the total binocular FOV to perceive immersive experience in VR is around 200°-220°. While an AR device does not need such a large FOV, because the real scene already occupies most of the observers' FOV. The virtual image is just need to be displayed within a specified region within the real scene.

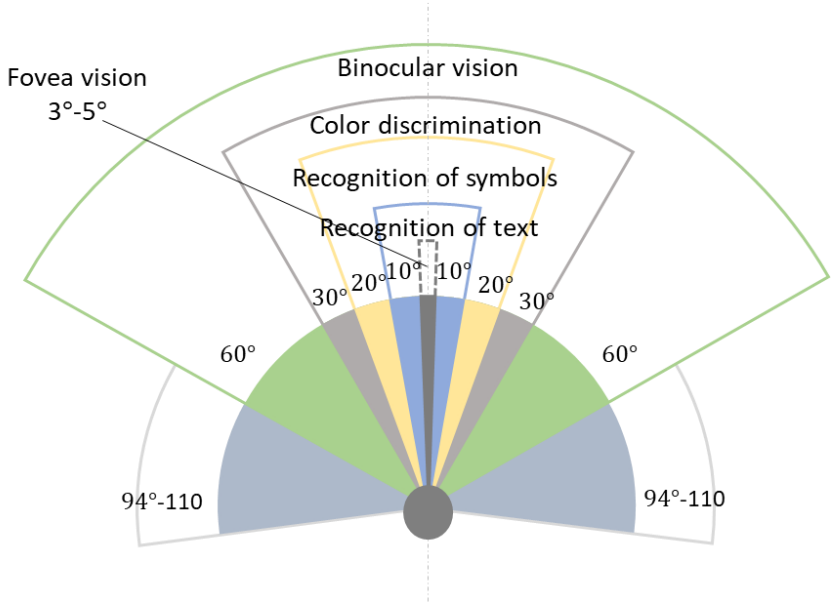

Figure 1.1 Features of human visual perception in accordance with FOV

Eyebox: The eyebox determines how much the eyeball can move up/down/left/right from the optimal position without significant degradation in the image quality. In a HMD system, the image quality at the optimal position is always the best, but if the eyebox is too narrow, the user will not obtain a good image without tedious adjustments [11]. In addition, the eyebox size should be decided in accordance with the FOV. For example, 10° eye rotation requires about 2 mm eye pupil shifting in the corresponding direction.

Aberration: Lenses and curved mirrors introduce a variety of optical aberrations [8-10]. Chromatic aberrations occur due to refractive feature of the lenses. Reflective optical elements such as concave mirrors do not induce chromatic aberrations. Considering that full-color displays only have RGB

components, chromatic aberrations can be compensated by separately predistorting R, G, and B planes at the expense of increased rendering costs. This technique greatly contributes to flexibility in optical designs, resulting, for example, in inexpensive wide FOV such as Oculus Rift. Spherical aberrations are induced by the spherical shape of the lens surface. With lateral shift of the eye, the image gets distorted and blurred. Similarly, field curvatures caused blurred imagery in the periphery. Rendering based predistorting technics are not effective to correct these aberrations. Instead, aspheric and/or achromatic lenses can be used.

Focus cues: Depth perception occurs with monocular and/or binocular depth cues. These cues can be further categorized into physiological and psychological cues [12-15]. Physiological monocular depth cues include accommodation, monocular convergence, and motion parallax. Psychological monocular depth cues include apparent size, linear perspective, aerial perspective, texture gradient, occlusion, shades, and shadows. Binocular convergence and stereopsis are typical physiological and psychological binocular depth cues, respectively. Binocular convergence is related to the angle between two lines from a focused object to the both eyes, while stereopsis is about the lateral disparity between left and right images. Although current generation VR displays provide some of the depth cues, however, focus cue is usually not supported. The decoupled focus cues and vergence, which is called vergence accommodation conflict (VAC) induces user uncomfortable physiological functions such as fatigue, double vision, and eyestrain. [12-17]. To display natural three-dimension (3D) images, researchers in academy and industry attempted to apply the existing 3D

display technics to the HMD systems for AR/VR. Some examples are as follows:

Recently, some researchers applied retinal projection technic: Maxwellian view display, to achieve a significant large depth of field (DOF) for binocular disparity based displays. The method has all-in focus effect because of the tiny exit pupil. As a result, this type display achieves the long DOF by losing the resolution of the displayed images. Furthermore, because of the all-in focus effect, in order to provide the focus cue, it requires artificial blur for the rendered images based on the user's convergence information.

Varifocal display is typically categorized into two types i.e. varying lens focal length [18, 19] and varying display position [20]. The former uses a varifocal lens such as liquid lens to focus the display at different focal distances depending on the user's fixation point. The latter dynamically translates the micro-display, which is mounted on a micro-controlled stage. Both of them require eye-tracking system that is capable of tracking the convergence of both eyes. In these methods, the latency between the electronic devices is the main issue to provide a natural varifocal images.

Light field display describes the radiance of emitted light rays as a function of both position and direction. The light field display can be categorized into three types: parallax barrier based multiview display [21-23], lens array based integral imaging display [24-28] and multilayer display [29-32]. They provide multiple directional view images by scarifying the spatial resolution of the display. Motion parallax is the dominant depth cue in the light field displays while the most important factor to alleviate the VAC of

the HMD is focus cue. To date, many studies have reported about light field based near-eye displays, however, there is no enough evidences to prove that the technic indeed provides 3D images in any desired depth plane.

All the 3D display techniques mentioned about have a common problem of providing sufficient focus cues to users. Compared with the other 3D display technics, holography is regarded as the most natural way to provide correct depth cues since it can reconstruct 3D images with full wavefront information [35-49]. Holography does not have any tradeoff and constraint in providing focus cues. The features of expressible depth range for the 3D display technics mentioned above are listed in Table 1.

Table 1.1Features of expressible depth range for 3D displays

	Trade-off (MTF vs. DOF)	Constraint
Maxwellian view	Yes	Yes (Exit pupil size)
Varifocal	No	Yes (Frame rate)
Light field	Yes	No
Holography	No	No

1.2 Motivation of this dissertation

To be a practical method for HMD, holography confronts several fundamental problems: 1. Form factor, 2. FOV, 3, Speckle noise. There are few studies about these issues. This dissertation introduces several methods that have been proposed targeting on these issues.

This dissertation introduces novel approaches using a multifunctional HOE to replace a beam splitter and an eyepiece lens in the conventional holographic display. In this study, I verified the feasibility of using HOE in the holographic display through some analyses based on Kogelnik's coupled-wave theory. The method can be contributed to building a compact see-through near-eye holographic display for AR [46, 47].

Furthermore, to build a wide FOV holographic HMD, I proposed two methods to increase the SBP of the display. The methods can effectively solve the trade-off between FOV and eyebox size in the conventional holographic display. Especially, the second one called *polarization selective holography* is a brand new method for hologram computation and encoding. It enables us to modulate two different holograms using different diffraction orders of a spatial light modulator (SLM) without any mechanical movements. Furthermore, a spherical hologram method of real objects is proposed. The method can be the basic computation architecture when curved SLMs are available in the future.

Last, for speckle noise issue, I introduce some analyses on the light source selection. To suppress the speckle noise, I measured the feasibility of using LED light source for a near-eye holographic display. An inherent

problem caused by use of the LED can be mitigated by using a magnifier optical system. This concept can be used as the basic model for the near-eye holographic display.

The ultimate goal of the dissertation is to propose some effective methods for developing more advanced near-eye holographic display.

1.3 Scope and organization

Chapter 1 gives an over view for the some important issues in near-eye displays and explains why the holography should be the ultimate technic in terms of focus cue ability.

In Chapter 2, a form factor reduction method is introduced using a multifunctional HOE. Before explaining the proposed idea, some optical characteristics of the HOE are measured to validate the condition to be met for using HOE in the holographic display. Then, I introduce the design and fabrication of the multifunctional HOE. A mirror and a lens are sequentially recorded on a single hologram recording material. To avoid the crosstalk between the two optical elements, the angles of the reference beam for the two signal beams are separated to a sufficient large angle. Last, a wavefront aberration method is proposed to precisely compensate the aberration caused by use of the HOE.

In Chapter 3, two SBP enhancement methods for holographic display are demonstrated. The first one mechanically divide an SLM's frame into three parts so that users can observe different reconstructed images through $+1^{st}$, 0^{th}, -1^{st} diffraction order of an SLM. The second method is named *polarization selective holography*. The principle, simulation and system implementation are introduced. Furthermore, a spherical hologram computation method considering occlusion effect is introduced in this chapter.

In chapter 4, different light source analyses on the reconstruction image quality is demonstrated. The LED is selected as the alternative to suppress

the speckle noise. Then, an optical design that mitigates the inherent problem for use of LED is demonstrated.

Finally, concluding remarks to this dissertation are presented in Chapter 5. The objective and the scope of this dissertation is depicted in Fig. 1.2.

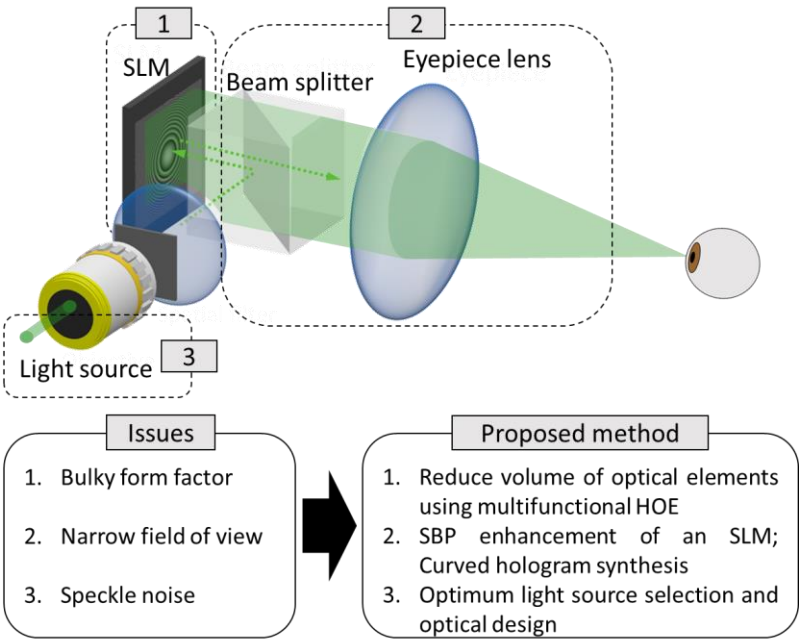

Figure 1.2 The objective and the scope of the dissertation

Chapter 2 Form factor reduction of near-eye holography using a multifunctional holographic optical element

2.1 Introduction of form factor issues in near-eye holographic display

A conventional holographic display consists of a liquid crystal on silicon (LCOS) SLM, a beam splitter and an imaging lens as shown in Fig. 2.1.

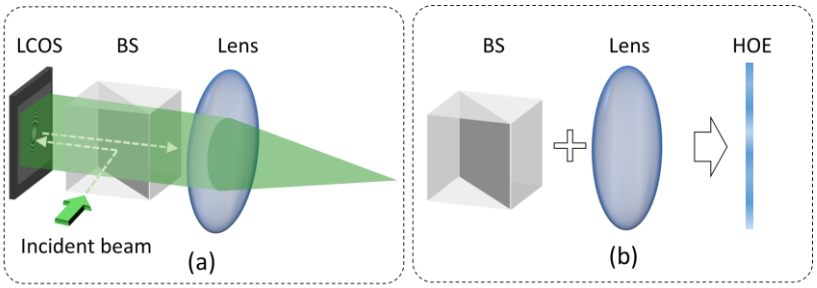

Figure 2.1 (a) Optical configuration of conventional holographic display. (b) Concept of the multifunctional HOE.

One of the important issues to realize a see-through near-eye holographic display is that the eyepiece part should be transparent and compact enough. As shown in Fig. 2.1(a), the configuration is unable to

provide a see-through effect. Thus, I propose a multifunctional HOE named with mirror lens HOE (MLHOE), which performs the functions of both beam splitter and lens at the same time. The properties of the HOE recording material enable us to use a transparent, lightweight, and thin optical element as the eyepiece lens.

This chapter introduces the see-through holographic display system realized by the MLHOE. First, I introduce the characteristics of a volume hologram, and analyze the condition to be met for using HOE for holographic display depending on the coupled-wave theory [51]. The fabrication of the MLHOE is also included in this chapter. Finally, the benchtop of the proposed system is demonstrated.

2.2 Introduction of volume hologram

Gratings behave differently depending on the relation between the period of the finest fringe and the thickness of the recording medium. According to the relation, it is generally categorized to thick or thin hologram.

If we consider a hologram consisting of a single sinusoidal grating with grating plane normal to the surface of the emulsion, it behaves as a thick or thin grating depending on the value of the Q parameter that is given by [51-54]

$$Q = \frac{2\pi\lambda d}{n\Lambda^2} \tag{2.1}$$

where λ is the wavelength of the light used in reconstruction process, n is the refractive index of the medium after processing, Λ is the grating period, and d is the thickness of the medium. If $Q > 2\pi$, the grating is considered as "thick", while for $Q < 2\pi$, the grating is "thin".

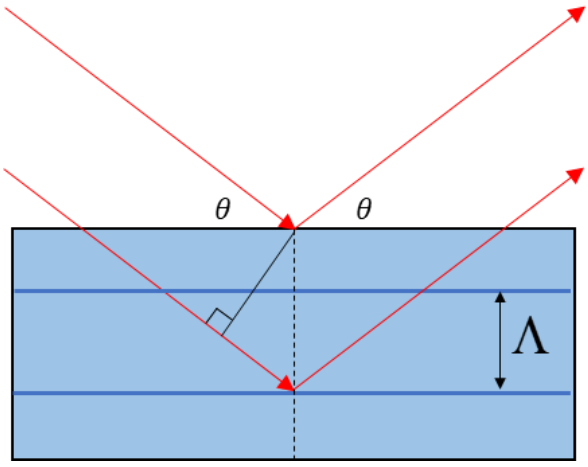

Figure 2.2 Diffraction in a volume grating

For gratings formed by two plane waves in a volume hologram, periodic index modulation induces an array of equidistant planes as depicted in Fig. 2.2. Let us assume that the number of these planes are infinite along horizontal direction. The planes can be regarded as specular mirrors, which reflect (scatter) the incident waves with the same angle. The scattered light consists of linear superposition of all these reflected plane waves. The diffracted beams are found when all these reflected plane waves add up constructively under the Bragg's law which is given by [51-54]

$$2d\sin\theta = n\lambda. \tag{2.2}$$

In a thin grating, the grating dimension in the transverse dimension is relatively small, compared with the wavelength of light, thus it acts as slits diffraction rather scattering. Thus, there are a series of diffraction orders for any given angle of incidence. On the other hand, the thick grating only has a single diffraction order. This is the main difference between a thin grating and a thick grating.

2.2.1 Diffraction efficiency: coupled-wave theory

The high diffraction efficiency of the volume hologram makes it practical to be used as various optical elements, which are called HOE. Two main factors for HOE design are diffraction efficiency and diffraction direction of the reconstruction beam. The former one can be analyzed by coupled-wave theory and the latter one can be analyzed by vector space diagram.

Coupled-wave theory is a useful theoretical basis to design the HOE

[51-54]. The Coupled-wave theory mainly consists of three steps. The first one is modeling of hologram gratings such as axes setting. In this dissertation, the *z*-axis is chosen perpendicular to the surface of the medium, the *x*-axis in the plane of incidence and parallel to the medium boundaries and the *y*-axis perpendicular to the paper as shown in Fig. 2.3.

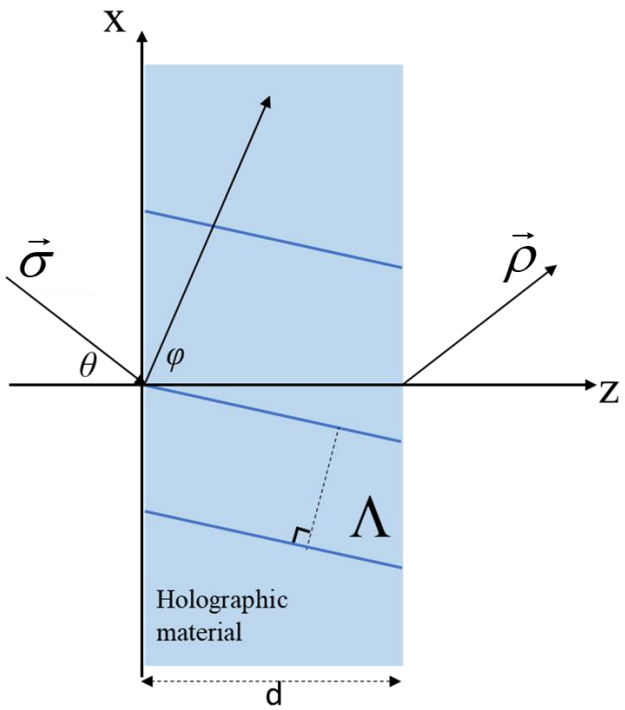

Figure 2.3 Model of diffraction in a volume grating.

The next step is deriving the coupled equations, which describes amplitude exchange between reference wave and diffracted wave by solving the Helmholtz equation of Eq. (2.3). Details of the derivations are beyond the scope of the thesis, so I only discuss the most important properties that

involve the diffraction efficiency of the volume gratings [51].

$$\nabla^2 E + k^2 E = 0, \tag{2.3}$$

where $E(x, z)$ is the complex amplitude of the y-component of the electric field, which is assumed to be independent of y and to oscillate with angular frequency ω. The wave number k is spatially modulated by reflective index and absorption constant which is given by

$$\begin{aligned} n &= n_0 + n_1 \cos \vec{K} \cdot \vec{r} \\ \alpha &= \alpha_0 + \alpha_1 \cos \vec{K} \cdot \vec{r}, \end{aligned} \tag{2.4}$$

where $\vec{K}$ is grating vector. The hologram is assumed to lie with its face parallel to the (x, y) plane and to be of thickness d in the z-axis. A number of assumptions are needed for simplification of solving the wave equation. First, it is assumed that the hologram is thick enough that the total wave field is expressed by summation of two complex amplitudes.

$$U(\vec{r}) = R(z)\exp(j \cdot \vec{\rho} \cdot \vec{r}) + S(z)\exp(j \cdot \vec{\sigma} \cdot \vec{r}). \tag{2.5}$$

The first term is gradually depleted by diffraction and absorption, the other is the first-order Bragg-matched grating order. The wave vector $\vec{\rho}$ is that of the probe wave in the absence of coupling, and that the wave vector $\vec{\sigma}$ of the diffracted wave is given by

$$\vec{\sigma} = \vec{\rho} + \vec{K} \tag{2.6}$$

The other assumptions are that absorption in a distance of one wavelength is very small and that the variations of the refractive index are

small compared to its mean. It is now possible to expand and simplify k^2 for use in the wave equation as follows:

$$\begin{aligned} k^2 &= \left[k_0 \left(n_0 + n_1 \cos \vec{K} \cdot \vec{r} \right) + j \left(a_0 + a_1 \cos \vec{K} \cdot \vec{r} \right) \right]^2 \\ &\approx \beta^2 + 2 j \beta a_0 + 4\kappa \cos \vec{K} \cdot \vec{r}, \end{aligned} \tag{2.7}$$

where, $\beta = k_0 n_0$ is the propagation constant, and κ is the coupling constant, given by

$$\kappa = \frac{1}{2} \left(k_0 n_1 + j a_1 \right). \tag{2.8}$$

By substituting the assumed solution Eq. (2.5) and the Eq. (2.7) into the wave equation Eq. of (2.3), we obtain the Coupled-wave equations, which are given by

$$\begin{aligned} c_R R' + a_0 R &= j\kappa S \\ c_s S' + \left(a_0 - \varsigma \right) S &= j\kappa R, \end{aligned} \tag{2.9}$$

where ς is called the "detuning parameter," measuring the extend of Bragg mismatch of the probe wave, which is given by

$$\varsigma = \frac{\beta^2 - \left| \vec{\sigma} \right|^2}{2\beta}. \tag{2.10}$$

The abbreviations c_R and c_S are given by

$$\begin{aligned} c_R &= \frac{\rho}{\beta} = \cos\theta \\ c_s &= \frac{\sigma}{\beta} = \cos\theta - \frac{K}{\beta} \cos\varphi, \end{aligned} \tag{2.11}$$

where θ and φ are defined in Fig. 2.3.

Diffraction efficiency of transmission grating

In the analysis for both transmission and reflection gratings, the absorption coefficients are set to $\alpha_0=\alpha_1=0$. For a transmission geometry, the boundary conditions to be applied to the differential equations Eq. (2.9) are $R(0)=1$ and $S(0)=0$. The solution for the diffracted wave S at the exit of the grating is obtained when $z=d$. The diffraction efficiency η, which is the energy ratio between probe wave and diffracted wave, is given by [51-54]

$$\eta = \frac{\left|S(d)\right|^2}{\left|R(d)\right|^2} = \frac{\sin^2\sqrt{\left(\nu^2+\xi^2\right)}}{\left(1+\xi^2/\nu^2\right)}, \tag{2.12}$$

where

$$\nu = \frac{\pi n_1 d}{\lambda\sqrt{c_R c_S}}, \tag{2.13}$$

$$\begin{aligned}\xi &= \Delta\theta K d\sin\left(\varphi-\theta_0\right)/\cos\theta \\ &= -\Delta\lambda\cdot K^2 d/8\pi n c_R\end{aligned} \tag{2.14}$$

Diffraction efficiency of reflection grating

For a reflection grating, the grating planes run nearly parallel with the face of the recording medium. The boundary conditions are changed to $R(0)=1$, and $S(d)=0$. Solution of the coupled-wave equations for the reflection grating now yields the following expression for the diffraction efficiency

$$\eta = \frac{\left|S(0)\right|^2}{\left|R(d)\right|^2} = \left[\frac{1+(1-\xi^2/\nu^2)}{sh^2\sqrt{(\nu^2-\xi^2)}}\right]^{-1}, \tag{2.15}$$

where

$$\nu = \frac{\pi n_1 d}{\lambda\sqrt{c_R c_S}}, \tag{2.16}$$

$$\begin{aligned}\xi &= \Delta\theta \cdot Kd \cdot \sin(\theta_0 - \varphi)/2c_S \\ &= \Delta\lambda \cdot K^2 d/8\pi n c_S.\end{aligned} \tag{2.17}$$

These expressions can again be used to formulate rules for the angular bandwidth and the spectral bandwidth of the grating.

2.2.2 Condition to be met for using holographic optical element in holographic display

Several simulations are carried out to measure the feasibility of using HOE in the holographic display. First, the diffraction efficiency distribution according to different grating formations is analyzed. In the simulation, the gratings are generated by different angles of signal and reference waves and each angle varies from 0 to π. Figure 2.4 shows the diffraction efficiency under Bragg-matched condition for transmission type and reflection type HOE. As shown in Fig. 2.4, the diffraction efficiency of transmission grating rapidly fluctuates according to different angles of reference and signal waves while that of the reflection one shows a good uniformity according to different angles of recording waves.

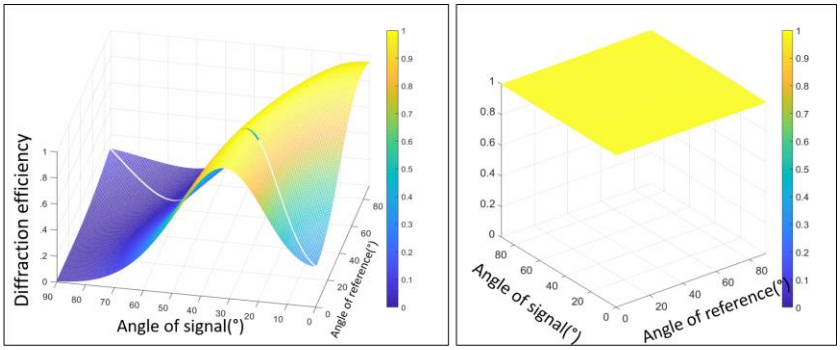

Figure 2.4 Diffraction efficiency distribution (Bragg-matched condition) according to the different angles of reference and signal waves. (a) Transmission grating and (b) reflection grating.

According to the simulation results, the reflection type HOE is more appropriate to be used in the holographic display for the flowing reasons. When one fabricates an HOE lens, the signal wave is a spherical wave, which means the k vectors of the signal wave vary within the range of the numerical aperture (NA) of the lens. The HOE lens should show the similar diffraction efficiency for k vectors of the signal wave. As shown in Fig. 2.4, however, the diffraction efficiency of the transmission grating rapidly varies depending on the angle of the signal wave. Therefore, transmission type gratings are not appropriate for HOE lens fabrication in terms of the diffraction efficiency uniformity. The second reason is the angular selectivity for the HOE. When a plane wave illuminates an SLM, the pixelated structure diffracts the plane wave within the diffraction angle of the SLM. It means that if one uses waves coming from the SLM as the probe wave, some

diffracted terms whose wave vector are deviated from the reference wave are Bragg mismatched to the HOE. If the angular selectivity of the HOE is sufficient, the deviated waves can be guided to the designed directions with a uniform diffraction efficiency. Thus, the bandwidth of the angular selectivity: $4\kappa d$ [53] should be larger than at least the diffraction angle range of the SLM. Therefore, if one wants to use the HOE for holographic display, it should satisfy following condition:

$$4\kappa d \geq \sin\left(\frac{\lambda}{p}\right)^{-1}. \tag{2.18}$$

The holographic material: photopolymer used in the experiments of the dissertation has 16 um width and the SLMs used for holographic display have 3.74 um and 8 um pixel pitches. As shown in Fig. 2.5, the reflection type HOE satisfies the condition of Eq. (2.18), while the transmission one does not.

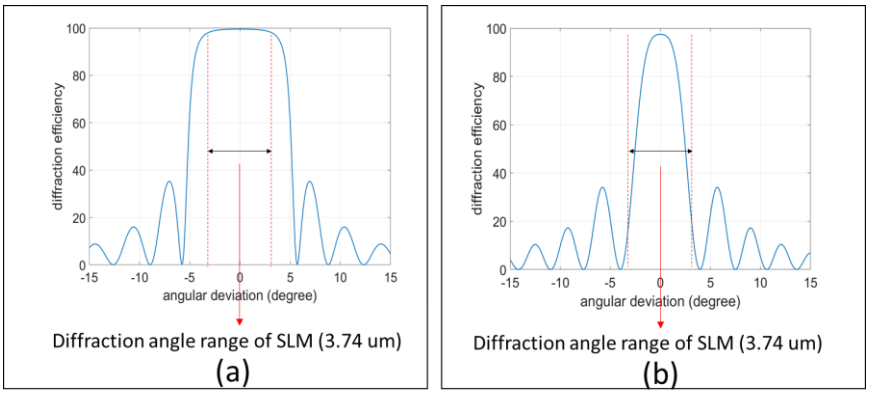

Figure 2.5 Angular selectivity of (a) reflection grating and (b) transmission grating.

Two additional experiments are carried out to validate the analysis mentioned above. The angle of reconstructed wave depending on the angular deviation of the probe wave is given by

$$\theta_c = \sin^{-1}\left\{\sin\theta_p + \sin\theta_s - \sin\theta_r\right\}, \tag{2.19}$$

where θ_c is the reconstruction wave's angle, θ_p is the angle of probe wave, θ_s and θ_r are the angle of the signal wave and reference wave used in the recording process, respectively. Figure 2.6 shows the experiment setup. The direction and the power variation of the reconstruction waves are measured by changing the probe wave from -10° to +10° about the Bragg-matched angle. In these experiments, the angle of the reference and signal waves are 45° and 0°, respectively. The angle of probe wave is changed by rotating the HOE, which is placed on a precise motorized rotation stage. A power-meter is used to detect the reconstructed wave position and the power. A diode-

pumped solid state (DPSS) laser with the wavelength 660 nm was used in the experiment.

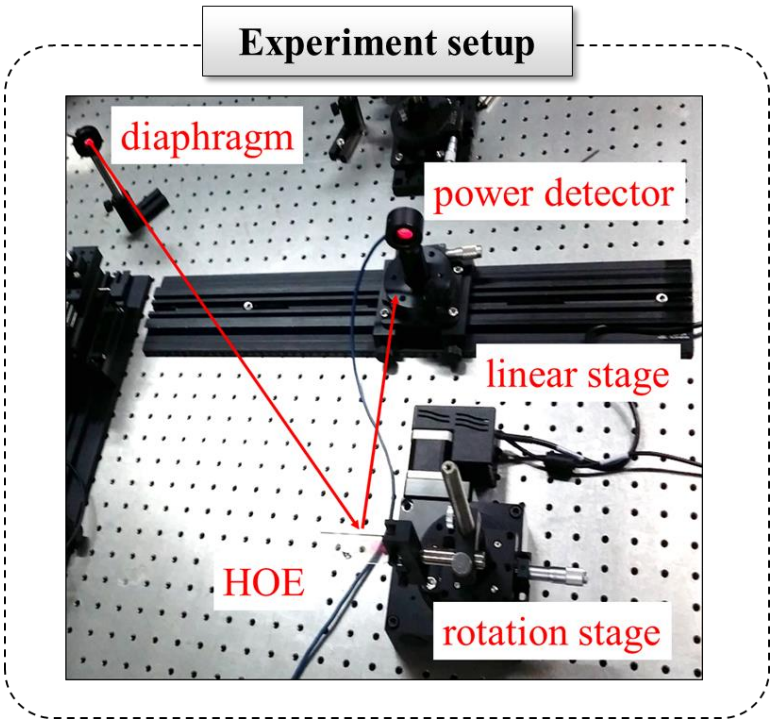

Figure 2.6 Experimental setup to validate the feasibility of HOE for holographic display.

Figure 2.7 shows the experimental results and corresponding simulation results. In Fig. 2.7(b), the diffraction efficiency distribution is calculated by Eq. (2.15) (diffraction efficiency of reflection volume grating).

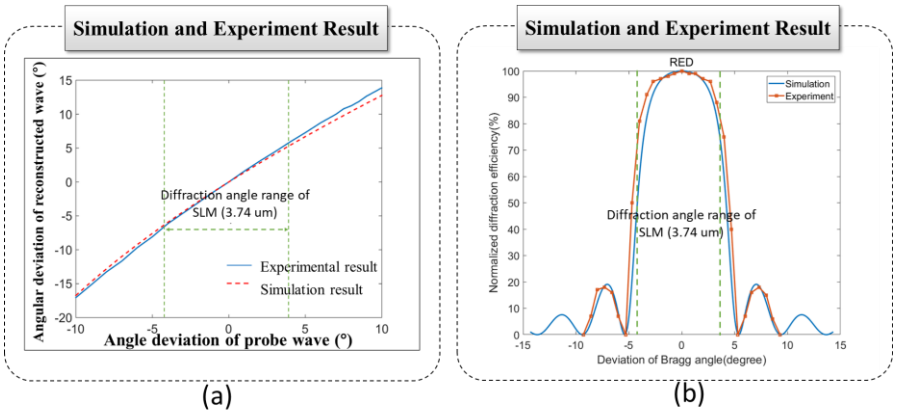

Figure 2.7 Experimental and simulation results to validate the feasibility of HOE for holographic display. (a) Angular deviation of reconstructed wave and (b) diffraction efficiency according to the angular deviation of probe wave.

Let us turn to the point why the HOE is more appropriate to be used in the holographic display rather than the other conventional display. As shown in Fig. 2.8, when a point light source is imaged by a normal lens, the angular resolution of the imaged point is determined by the diameter d_L of the lens. The angular resolution is given by

$$\sin\varphi = 1.22\frac{\lambda}{d_L}. \tag{2.20}$$

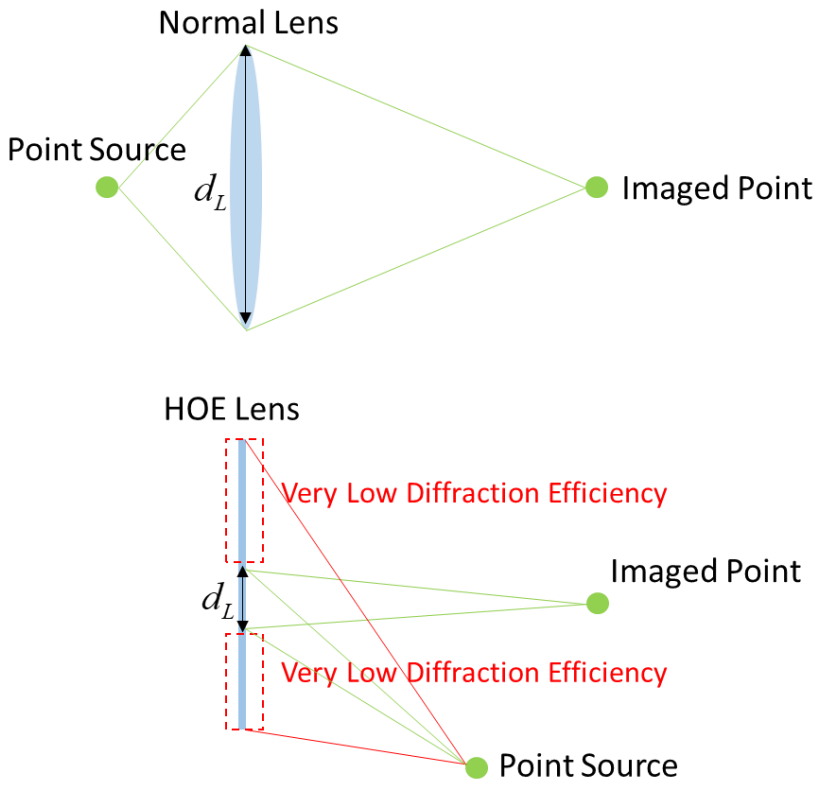

Figure 2.8 Resolving power comparison between a normal lens and an HOE lens.

From Eq. (2.20), the effective diameter d_L in the HOE lens is generally smaller than that of the normal lens because of the angular selectivity. Even if we neglect the aberration factor, an HOE lens has worse resolving power than a normal lens. As shown in Fig. 2.8, only limited range in the HOE lens performs as a desired lens function with a high diffraction efficiency.

The other reason is the severe aberration of HOE lens. As shown in Fig. 2.9, due to the off-axis HOE recording geometry, the wavefront curvature

ratio in the vertical and horizontal directions are different, which means it suffers from severe astigmatism aberration. In addition, there are some high-order aberrations caused by the optical elements alignment in the HOE recording and reconstruction systems. As a result, many kinds of aberrations occur when the HOE lens is used in the imaging system. The HOE lens is hardly used in an imaging system because of the difficulty in aberration compensation. On the other hand, the holographic display is wavefront modulation based display, so it can conveniently compensate the aberrations by just modifying the contents. Furthermore, both the HOE and holographic display use the same light source. Considering all these reasons mentioned above, holographic display is the ideal system to use HOEs as the optical element.

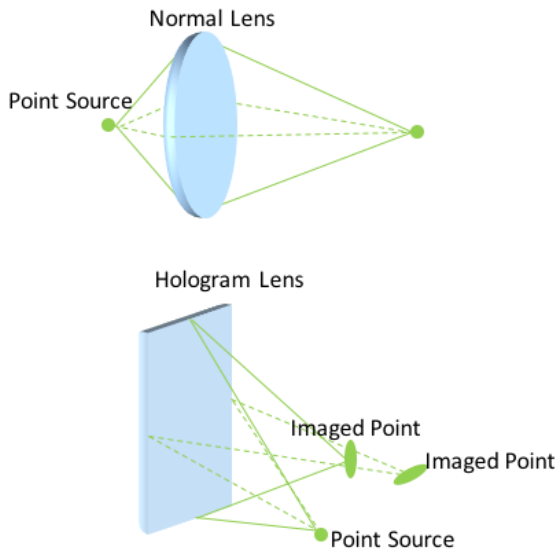

Figure 2.9 Aberrations comparison between a normal lens and a HOE lens.

2.3 Multifunctional holographic optical element fabrication and application

2.3.1 Design of mirror-lens holographic optical element

The procedure of the MLHOE recording and reconstruction are illustrated in Fig. 2.10. Based on the angular multiplexing characteristics of volume hologram, I record two optical elements in a single holographic recording material using different recording angles. In the first step, a plane signal wave (S1) and a plane reference wave (R1) are used to record a mirror function HOE. In the second step, a spherical signal wave (S2), which is produced by a lens, and a plane reference wave (R2), are used to record a lens function HOE at the same recording material [46].

In the reconstruction process, a probe wave, which is identical to the R1, illuminates the fabricated MLHOE. The HOE diffracts the R1 to the SLM with the direction of S1. Then, the wave modulated by the SLM is used as the second probe wave R2′ to illuminate the HOE. Finally, the HOE performing a lens function converges the beams from SLM into MLHOE's focal point, which is indicated as S2′. Note that, except the reasons mentioned in the previous section, the other reason of using reflection type HOE is to put the light source at the same side with observers to avoid un-diffracted laser beam directly coming into users' eyes.

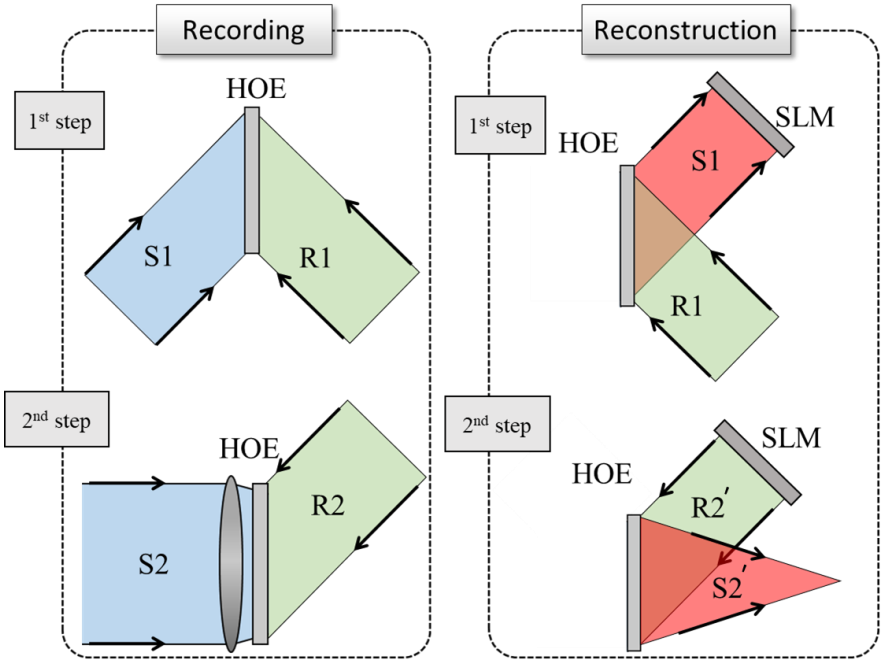

Figure 2.10 Schematic diagram of the MLHOE recording and reconstruction procedures.

In order to implement a see-through holographic AR display, the optical axes of SLM and observing direction should be located in off-axis. Therefore, the waves from the SLM illuminates the MLHOE with an oblique angle. A measurement is carried out to investigate the aberration caused by tilted probe wave of the MLHOE, and the experiment result is illustrated in Fig. 2.11.

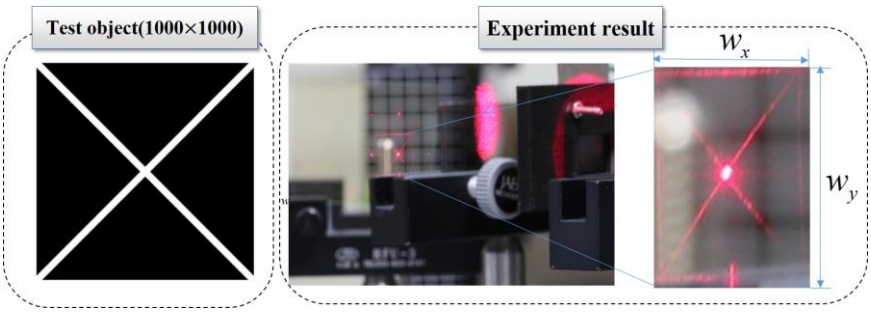

Figure 2.11 Experiment to investigate aberrations of HOE lens in hologram reconstruction procedure.

The hologram of a test pattern shown in the Fig. 2.11 is reconstructed in the experiment. In Fourier hologram, the spatial spectral bandwidth is in inverse proportion to the pixel pitch of the SLM. In normal case, the size of viewing window of reconstructed hologram should be the same in horizontal and vertical directions. The size of the viewing window along both the directions are defined as $w_{x,y}=\lambda f/p_{x,y}$, where λ is wavelength of light source, f is focal length of Fourier transforming lens, and p_x and p_y are pixel pitches of SLM in the horizontal and vertical directions, respectively [36]. However, the viewing window is not a square shape when I use the MLHOE to reconstruct the Fourier hologram as shown in Fig. 2.11. From the experiment, the ratio of the viewing window size in horizontal and vertical directions is measured as $w_x:w_y=\cos\theta:1$, where θ ($\theta<90°$) is the angle of R2′. It means that the wavefront from the SLM indeed have aberrations such as astigmatism after being diffracted by the MLHOE. In order to reconstruct the desired wave field, I need to conduct a wavefront compensation method to the hologram, which is introduced in the section 2.3.3.

2.3.2 Fabrication of mirror-lens holographic optical element

There are various kinds of holographic materials for implementing the HOE: the silver halide, photorefractive polymer, photopolymer, and so on. [55-60]. Among them, since HOEs implemented on the photopolymer have a thin, transparent and high diffraction efficiency, many studies have been reported using photopolymer based HOE to be transparent image combiners for AR devices. [59-64].

In the case of recording two holograms in a single HOE, the exposure energy of each one should be appropriately adjusted to achieve the similar diffraction efficiency. For this reason, diffraction efficiency distribution according to gradually increased exposure energy is measured as shown in Fig. 2.12. During the HOE recording process, interference patterns between signal and reference waves are stored in the photopolymer by modulating its transmittance or refractive index. Exposed light on the interference pattern activates the monomers to polymers. Finally, the difference of the refractive index between the polymerized area and the original material leads to the modulation of refractive index. Therefore, if the same amount of monomers can react for recording each optical element, it is possible to make balanced diffraction efficiencies between them. The optimized exposure energies for the two steps are determined based on the measured data shown in Figure 2.12.

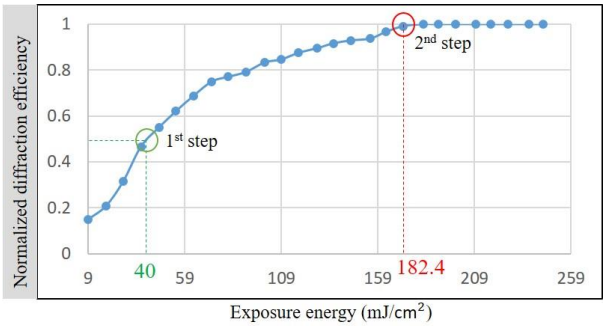

Figure 2.12 Diffraction efficiency distribution according to exposure energies.

As shown in the result, the diffraction efficiency rapidly grows as the exposure energy increases at the beginning, and then the diffraction efficiency gradually reaches saturation. The diffraction efficiency (η) can be calculated by Eq. (2.21)

$$\eta = \frac{I_D}{I_T + I_D}, \tag{2.21}$$

where I_D and I_T represent the power of diffracted and transmitted waves, respectively. The energy absorption and reflection on the photopolymer and substrate are neglected in this analysis. As shown in Fig. 2.12, in order to get 50% diffraction efficiency for each one, the exposure energy of the first step (marked in green) is set to 40mJ/cm^2 and that of the second one (marked in red) is over 182.4mJ/cm^2, which is the saturation energy level of the photopolymer.

The other issue in recording multiple optical elements in a single HOE by angular multiplexing technique is that the angle of two probe waves should be sufficiently separated to prevent crosstalk of two optical elements.

The probe waves used in the two steps are set to ±45° about the normal of the photopolymer. Figures 2.13(a) and (b) illustrate the experimental setup for recording the mirror HOE and the lens HOE, respectively. Since the recording conditions in the two steps are different, mirror 1(M_1) and mirror 3 (M_3) are set to be adjustable. A precise rotation stage on a linear stage is used to handle the position and the angle of M_1, which provides the signal waves for both steps; a rotation stage is used to adjust the angle of M_3, which provides the reference waves of both steps. The principle angles of S1 and S2 are 45° and 0° to the normal of photopolymer, respectively. The focal length of the lens that provides spherical signal wave is 300 mm. A plano-convex lens is used in the second recording step of the MLHOE. It is better to make the plane wave go into the convex side of the lens and spherical wave come out from the flat side, because the aberration of the doublet lens is only compensated along a single direction. In addition, since the S2′ is a converging spherical wave, the region of the recorded gratings increases by putting the HOE closer to the lens. Therefore, the photopolymer is placed very close to the flat side of the plano-convex lens in the actual practice.

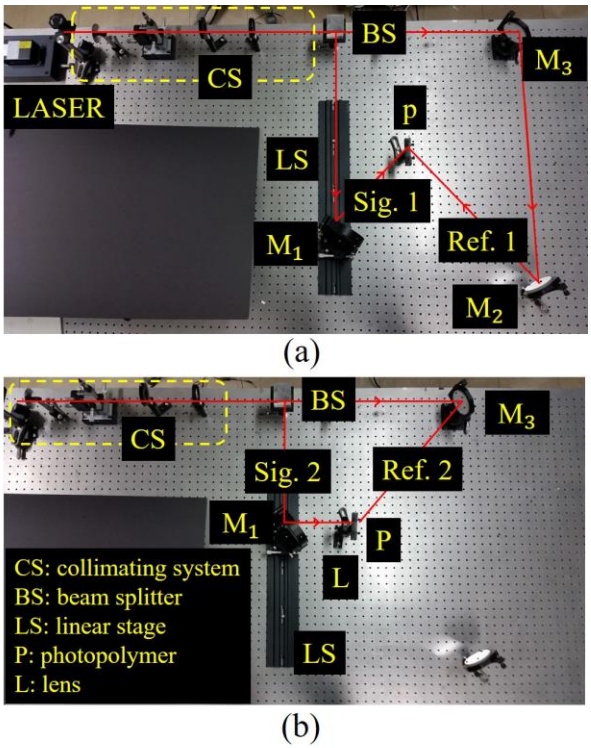

Figure 2.13 Experiment setup for (a) the 1st step and (b) the 2nd step of the MLHOE recording process.

2.3.3 System implementation and experimental results

Figure 2.14 shows the photograph of the prototype holographic AR display system. R1 satisfying the Bragg condition of the mirror HOE is the light source, and then S1 is diffracted to the reflection type SLM. As shown in Fig. 2.14, the real-world scene, which does not satisfy Bragg-matched condition, can be clearly observed through the transparent MLHOE.

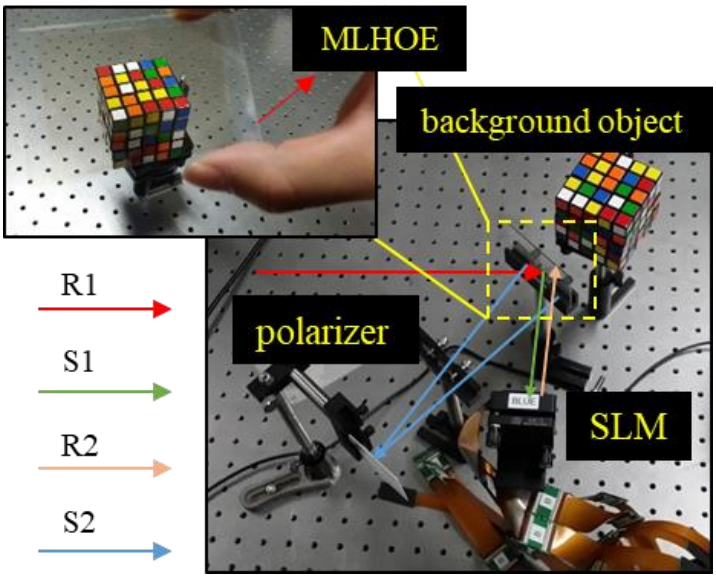

Figure 2.14 Prototype of the compact holographic display using MLHOE.

A DPSS laser with the wavelength 660 nm is used as the light source for all the experiments. The SLM, which is disassembled from a Sony VPL-VM300ES projector, is used as the SLM in the holographic display. The number of the pixels is 4096×2160 and the pixel pitch is 3.74 μm. In general, SLMs used in projectors are manufactured for amplitude modulation, thus it is better to use an amplitude type CGH encoding scheme in the experiments [65-67]. Two polarizers, which are orthogonal to each other, are placed in front and rear sides of the SLM, so that the SLM can work in amplitude mode. A half-band filter is positioned in the Fourier plane, so that the DC and conjugate terms can be eliminated. Figure 2.15 shows the resultant holograms with the real-world scene captured using the proposed holographic AR display.

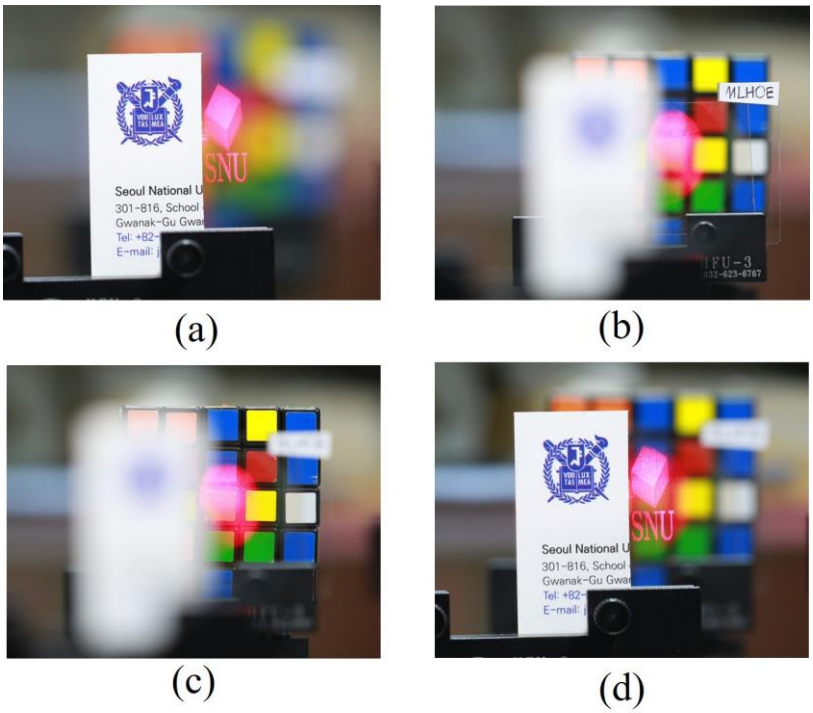

Figure 2.15 Experimental results: camera focus at (a) the Fourier plane of the SLM, (b) the MLHOE, and (c) the real object “Rubik’s cube,” (d) Camera is set to have a large depth of focus.

The CGH of the polygon object “Cube”, which consists of triangular meshes, is calculated by using the algorithm proposed by Matsushima *et al*. [68-70]. Depending on the relative position of each triangle aperture with respect to hologram plane, all the triangle meshes’ angular spectrum are calculated and mapped in the Fourier domain by 3D coordinates rotation and shift. In the reconstructed images, the distance between center of “CUBE” and the letter “SNU” is 3 mm, and “SNU” is reconstructed at the Fourier plane in which the half band filter (a business card) is located. The

accommodation effect is demonstrated at four different foci. In Figs. 2.15 (a)-(c), the camera is focused at the Fourier plane, MLHOE and the real-word object “Rubik’s Cube”, respectively. Figure 2.15(d) is captured with an enlarged DOF, so that the reconstructed holograms and the “Rubik’s Cube” can be observed in one scene. The experimental results verify the MLHOE can function as multiple optical elements to reduce the form factor of the conventional holographic display system. Furthermore, the transparent characteristics of the photopolymer enables us to get a see-through observation condition.

2.4 Wavefront aberration compensation method for holographic optical element

The Zernike polynomial functions are convenient way to characterize intuitive optical defects such as defocus, astigmatism, coma and distortion etc. [71,72]. An HOE lens for imaging system generally has severe aberrations because of the recording condition. Thus, aberration compensation is an essential process if one wants to use HOE as the imaging optical elements. In holographic display, since the SLM modulates the wavefront to reconstruct desired optical field, it is convenient to compensate wavefront aberrations. Prerequisites for carrying out the pre-compensation is acquisition of the wavefront information of the HOE. Digital holographic capturing technic is a well-known method to optical field acquisition method.

There are generally two different optical configurations for the digital hologram capturing: off-axis and in-axis configurations. The off-axis geometry is an effective configuration for separating the zeroth-order light and the twin image [74-76]. However, it is difficult to record a high-quality off-axis Fresnel hologram because of the limitation of the narrow bandwidth of the CCD. Thus, the resolution of the reconstructed optical field is not high. On the other hand, if the on-axis geometry is employed, it is necessary to eliminate the DC term and the twin noise [74]. Among the various available techniques, phase-shifting holography is the most widely used technique to achieve the optical field of the target wave. To get a sufficient good result, a three or four steps phase shifting technique should be used.

In this work, I use the on-axis digital holography technique based on

three-step phase shifting terferometry (PSI) to acquire the wavefront of the HOE. This interferometer system records three interferograms with modulating phase of reference wave. In doing so, irradiance of Newton's ring-shaped interference pattern is captured by a CCD camera. From three captured interference patters, the phase information can be recovered through a simple calculation. The calculated value of phase is only represented within 2π period due to the periodic property of sinusoidal function. The phase delay of lens actually exceeds the range 2π and is continuous. Therefore, the physically continuous phase variation of lens is required to be reconstruct by the unwrapping processing. The unwrapped phase can be expressed using Zernike polynomials that are efficiently used to represent optical wavefront aberration of circle-shaped lens. The correction wavefront is constructed by conjugating to aberration term of the Zernike polynomials. The phase used for the compensation is modulated by an SLM, which displays images with gray-scale value corresponding to the phase of correction wavefront before passing through the Lens HOE (LHOE). As a result, the modulated wavefront contains only optical property of lens and aberrations of the LHOE are eliminated after passing through the LHOE. It is possible to form a sharp focus spot which is similar to a conventional lens. We expect that the proposed method can mitigate the degradation of image quality by wavefront aberration.

To check the feasibility of the proposed method, I implemented the experimental setup, which consists of a 532 nm green laser source, an LHOE, a phase SLM, a beam splitter, mirror mounted on a piezo actuator and a CCD camera as shown in Fig. 2.16. I used a 532 nm green laser for the coherent

light source. The effective size of CCD is 10 mm (*H*) × 8 mm (*V*), the number of pixels is 2448 (*H*) × 2048 (*V*) and pixel pitch is 3.45 um. The SLM is an LCoS (liquid crystal on silicon) reflection type that can modulate the phase of input beam from 0 to 2π, which has a size of 15.3 mm (*H*) × 8.98 mm (*V*) and a resolution of 4094 (*H*) × 2400 (*V*).

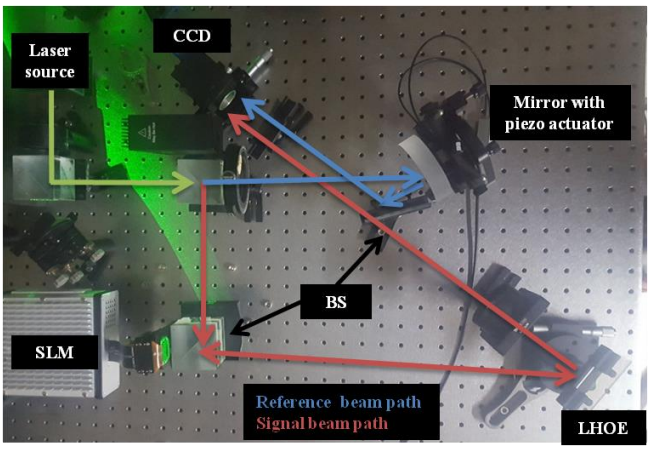

Figure 2.16 Experimental setup.

The interferometer for the wavefront detecting experiment took the form of a Mach-Zehnder interferometer. To control the phase of reference wave, a piezo-electric actuator is attached to the mirror in the optical path through which the reference beam passed. A piezo actuator is the optical element that converts a high voltage signal into a physical displacement in sub-wavelength units. The movement of mirror is precisely controlled to correspond to a specific phase value for solving the three-step phase shifting algorithm. For example, the phase differences (φ) between the reference and the signal waves are $-\pi/3$, π, $+\pi/3$ that are mainly used in three-step PSI. The

optical path difference (OPD) is a value corresponding to 88 nm mirror movement back and forth from any reference point. The interference fringe pattern of the reference and the signal wave is captured by the CCD camera in the form of Newton's ring, and the brightness of the concentric ring changes according to the phase difference of the two beams. The CCD is placed with on-axis line to the interference pattern. The wavefront phase of the LHOE at the CCD detection position is extracted by the following formula by using irradiance (I_n) of three interference patterns captured by CCD.

$$W_{sig} = \left\{ I_0 + I_1 \exp\left(i \frac{2\pi}{3} \right) + I_2 \exp\left(i \frac{4\pi}{3} \right) \right\} / 3, \tag{2.22}$$

The original wavefront of LHOE can be found by numerical back-propagation of the calculated wavefront at the CCD location based on angular spectrum method. The wavefront propagation is simulated using MATLAB software to find the wavefront at position of the LHOE. To recover the physical phase of LHOE wavefront, the 2D Goldstein phase unwrapping algorithm is applied to the removal of inherent 2π ambiguity. Figure 2.17(a) and (b) show wrapped phase and the Zernike polynomials extracted from the unwrapped phase. The vertical astigmatism is as shown in Fig. 2.17(c).

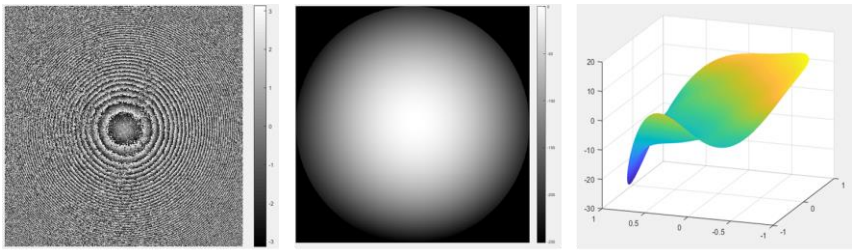

Figure 2.17 (a) Extracted phase of LHOE (b) Zernike polynomials (c) Zernike polynomials of aberration term.

Figure 2.18 shows the Zernike polynomials of correction wavefront that compensates the wavefront aberration of the LHOE. In order to modulate by using a SLM, the phase of the correction wavefront is required to convert to an 8-bit grayscale image as shown in Fig. 2.18(c).

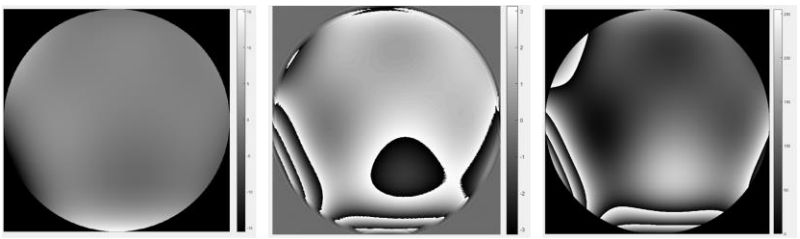

Figure 2.18 Zernike polynomials of correction wavefront (b) phase of wavefront (c) converted gray-scale image.

Figure 2.19 shows the captured image of point spread function (PSF) at the focal distance. Through these results, we confirm that the correction wavefront has a smaller and sharper PSF than the uncompensated wavefront.

Through the experiments, the feasibility of the proposed method is verified and it is numerically confirmed that the aberration of LHOE on Bragg mismatching condition is relatively higher than that on Bragg matching by using a Zernike polynomials, as shown in the Table 2.1.

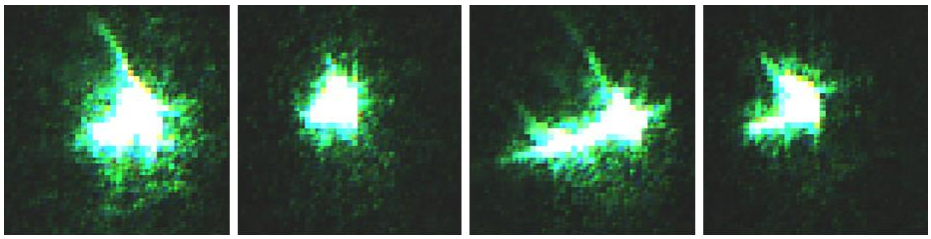

Figure 2.19 PSF images (a) before compensation on Bragg matching (b) after compensation on Bragg matching (c) before compensation on Bragg mismatching (d) after compensation on Bragg mismatching.

Table 2.1 Zernike polynomial coefficients of compensation

Noll index (j)	Classical name	Bragg matching (θ_i = 45°)	Bragg matching (θ_i = 46°)
Z_5	Oblique astigmatism	0	-2
Z_6	Vertical astigmatism	-10	-12
Z_7	Vertical coma	0.3	-0.7
Z_8	Horizontal coma	0.2	0.5

The proposed method is possible to compensate aberration caused by physical deformation such as shrinkage or shear of the HOE after recording process. In the experiments, the wavefront of off-axis HOE is precisely measured by using PSI. The result of wavefront propagation simulation using experimental data shows consistent results of actual case. Lasty, it shows that wavefront aberrations are efficiently removed by applying the correction wavefront.

2.5 Summary and discussion

In summary, an image combiner, which is realized by a multifunctional HOE is proposed to reduce the form factor of the holographic display. The single image combiner called MLHOE performs the optical functions of a mirror and a lens at the same time. Before fabricating the proposed MLHOE, I analyzed the feasibility of using HOE for holographic display based on the coupled-wave theory. The optical characteristics of the hologram recording material (photopolymer), supports the validity of the MLHOE for a see-through near-eye holography.

In addition, the wavefront aberration of the system can be conveniently compensated by only modifying the CGH, since holography is basically a display that controls the wavefront of light. To extract the wavefront information of the HOE lens, I use a digital holography technique to capture the fringe pattern generated from the HOE; and the obtained Zerinike coefficient enable us to compensate the CGH.

Furthermore, it could be possible to implement a full-color holographic AR display system by using a high speed framerate SLM and a color HOE which is recorded by three (red, green, blue) lasers. I expect the proposed method can be a solution for developing a compact see-through holographic AR displays such as holographic HMD and head up displays.

Chapter 3 Field of view expansion of near-eye holographic display

3.1 Overview of field of view expansion for near-eye holography

3.1.1 Investigation on constrains in expanding field of view for near-eye holography

In holographic display, diffraction angle of an SLM determines the FOV, which is defined by

$$\theta = \sin^{-1}\left(\frac{\lambda}{p}\right) \tag{3.1}$$

where λ is the wavelength of light source, and p is the pixel pitch of the SLM. So far, the pixel pitch of commonly used SLMs for holographic display is around 3.5 um - 12 um [39-47]. Thus, the FOV of the conventional holographic display is generally less than 10°. As shown in Fig. 3.1, the optical designs used for near-eye holography can be divided into two types: pupil relay and beam converging.

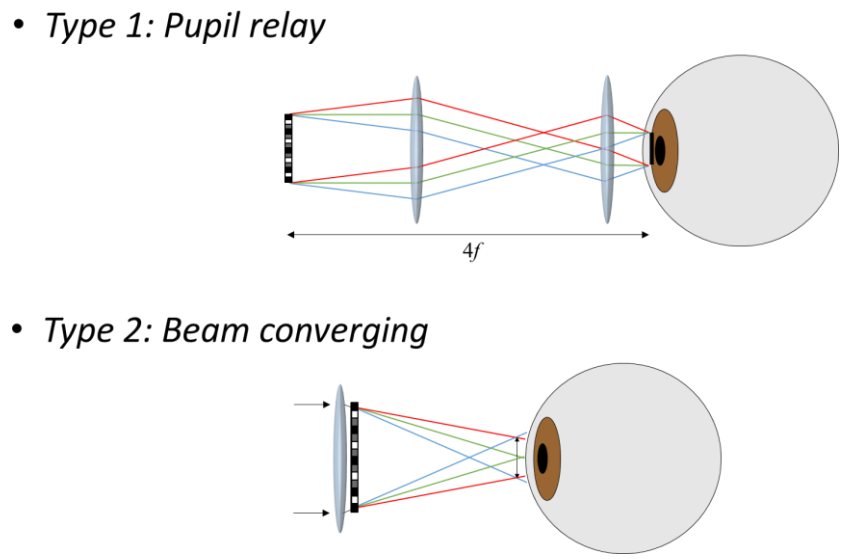

Figure 3.1 Optical designs for near-eye holography.

In the pupil relay method, a 4-*f* system is used to relay the de-magnified SLM to the pupil of the observer. To get a wider FOV, the SLM is generally demagnified based on the magnification between the two lenses used for the 4-*f* system. In this case, the diffraction angle θ of the SLM determines the FOV; and SLM size determines the eyebox. It means FOV, which is determined by bandwidth of the display is inverse proportional to the pixel pitch *p*; and eyebox size, which is determined by spatial size of the display is proportional to *p*.

On the other hand, in the second case, all the relations are reversed. In this case, the FOV is determined by the space size, which is proportional to *p*; and eyebox size is determined by the bandwidth, which is inversely proportional to *p*. The viewing characteristics of the two kinds of near-eye holography are listed in Table 3.1, where p' shown in the table is pixel pitch

of the demagnified SLM.

Table 3.1 Definition of the FOV and eyebox size in the two types of near-eye holography.

	FOV	Eyebox size
Pupil relay	$\sin^{-1}(\lambda/p')$	$p'\times n$
Beam convergence	$\tan^{-1}(p\times n/f)$	$\lambda f/(2\times p)$

As shown in Table 3.1, the FOV and eyebox size always have tradeoff relation. Recent trend for expanding the field of view is by sacrificing the eyebox size i.e. to reduce the effective pixel pitch of the SLM [50]. The schematic diagram and the experiment setup are illustrated in Fig. 3.2.

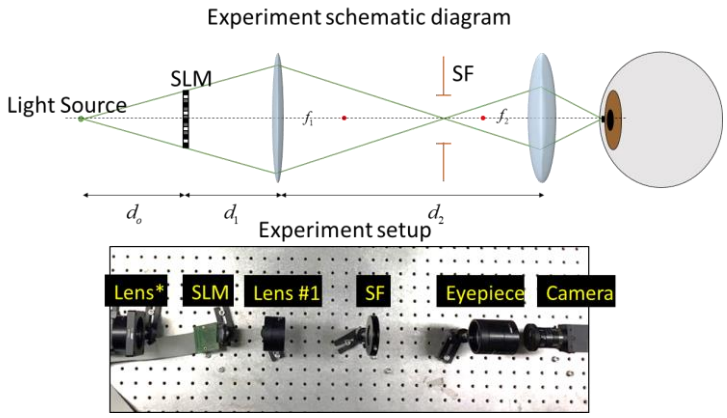

Figure 3.2 Experiment schematic diagram and setup of a wide FOV near-holographic display.

An SLM with 8 um pixel pitch and 1920×1080 pixel number, which is disassembled from an Epson projector, is used to display the CGH. A set of polarizers are placed perpendicular to each other so that the SLM can function as the amplitude mode. A lens placed before the SLM is used to produce a spherical reference wave to the SLM. A high power lens with 50 mm focal length is used as the eyepiece lens. The configuration of the system enables us to get a 50° FOV and 1.2 mm eyebox.

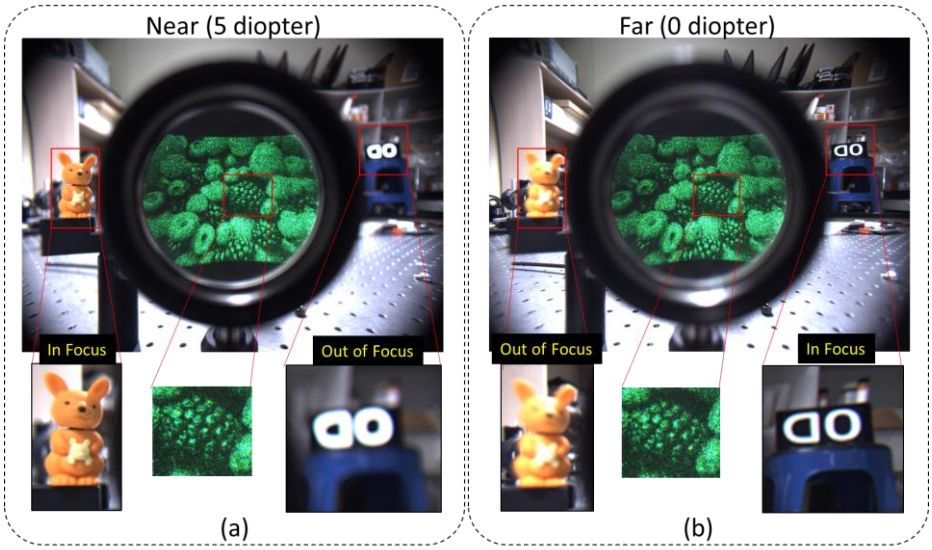

Figure 3.3 Experimental results: (a) reconstructed image when the camera focuses at 5 diopter. (b) Reconstructed image when the camera focuses at 0 diopter.

Figure 3.3 shows the captured images through the experiment. The result shows us that even if the camera focus changes from 5 diopter to the infinity, the reconstructed image still maintains the same resolution, which is

called all-in focus. If the eyebox size is reduced to a certain criterion, the DOF becomes very long, which is the same as the Maxwellian view. As a result, the display loses the accommodation effect. Therefore, the eyebox size should not be reduced arbitrarily for FOV expansion. Figure 3.4 shows the variation of FOV and DOF depending on different size of the eyebox. In this analysis, the pixel pitch of the SLM is specified as 8 um.

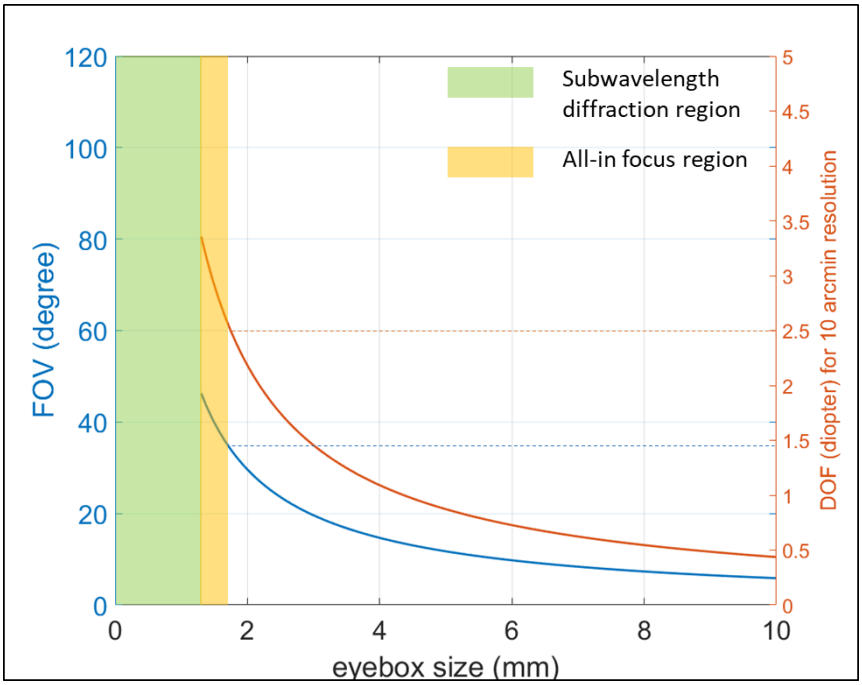

Figure 3.4 FOV and DOF variation according to eyebox size in holographic display. (SLM pixel number: 1920×1080, pixel pitch 8 um)

In the region marked in green, the pixel pitch of the SLM is reduced to be a subwavelength scale. Thus, we cannot use the conventional diffraction theory in this region. In the region marked in yellow, the eyebox size

satisfies the all-in focus condition so it loses the accommodation effect [77-80]. In summary, the maximum FOV that we can get by reducing the eyebox size is about 37° (SLM: 1920×1080 pixel number & 8 um pixel size). The FOV cannot be expanded without losing the size of eyebox if the pixel number i.e. SBP, is fixed. For an AR display system, the FOV is not supposed to be very large, because the real scene already occupies the majority FOV. Let us assume the necessary FOV is 30°. In this case, a reasonable eyebox size should be 6 mm so that it can support eye rotation in the FOV range. In this case, if we use an SLM having 1920×1080 pixel number and 8 um pixel pitch, the SBP should be enlarged 3 times.

Therefore, to solve the fundamental problem of FOV issue, the SBP must be enhanced. In the next section, I introduce the previous SBP enhancement methods and two novel proposed methods using high-order diffraction of an SLM.

3.1.2 Previous space bandwidth product enhancement methods for holographic display

SBP is an appropriate metric to evaluate the quality of holographic display. The SBP of a holographic display is defined as the product of the physical dimension and the corresponding 2D bandwidth of the display.

Several studies were carried out for obtaining a high SBP to alleviate the issues about FOV and viewing window in the conventional holographic display i.e. “far-eye holography” [36-42]. A common way to achieve the high SBP is using plural SLMs in a system. A typical method that tiles multiple

SLMs without gap between the adjacent ones, is arranging them at both sides of a sufficient large beam splitter with regular intervals [36, 37]. Fukaya *et al*. demonstrated a viewing angle enlarged holographic display by tiling three SLMs in Fourier hologram configuration. Later, the system was improved by tiling five SLMs with more pixel counts. Kozaki *et al.* proposed a wide viewing angle holographic display system using numerous SLMs in a curved structure [38], which does not need a large size Fourier transforming optics to cover all the SLMs. Han *et al.* also proposed a holographic stereogram system using curved array of a number of SLMs [39]. In this method, in order to remove the gaps resulted from pupils of the transfer lenses, three sub-regions of an SLM were rearranged to be positioned in contact with each other diagonally. Actually, the SBP of a single SLM was not increased because the pixel count in the vertical direction was sacrificed. Other methods for enlarging the viewing angle of the holographic display, which focused on naked eye observation, were proposed [40, 41]. Yaras *et al*. implemented one of the systems by tiling 9 SLMs; Kozaki *et al.* demonstrated another one by using additional SLMs placed in a specified image space. When a large size object is reconstructed in a small size viewing window, only a certain part of the object can be observed at a view point. Furthermore, several methods that arrange multiple 4K×2K-pixels SLMs in a planar structure to increase the size of viewing window were reported [43, 44]. For all the methods mentioned above, the inevitable problem is need of a large number of SLMs. In fact, considering cost, volume and alignment of the system, using a lot of SLMs to achieve a high level SBP is difficult to be an ultimate solution. Thus, how to increase the

SBP for a single SLM is one of the most important issues in near-eye holographic display.

3.2 Temporal multiplexing of high-order diffraction guided by holographic attenuating mirror

In this section, the SBP improvement of a single SLM in the holographic display is proposed by using multiple diffraction orders. The principle of the proposed method is illustrated in Fig. 3.5. The adopted diffraction orders are arranged with the same intensity and propagation direction using guiding optics and temporal-multiplexing system, so that a several-fold increase in SBP of a single SLM is achieved. The guiding optics system consists of HOE and a set of relay lenses. The HOE, which functions as both attenuator and mirror, enables us to adjust both the intensity and propagation direction of the reconstructed beams. Thus, the guiding optics system can be simplified by utilizing the features of HOE. Meanwhile, the relay lens system is used for obtaining a seamless arrangement of the guided terms.

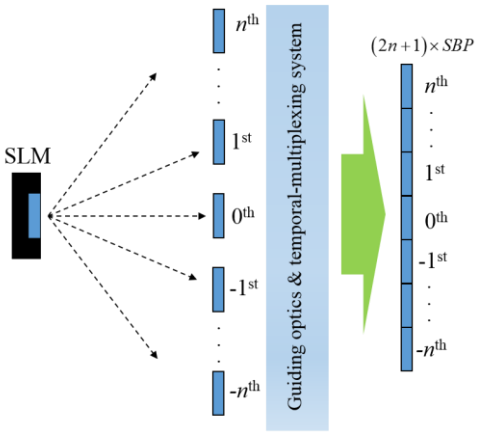

Figure 3.5 Schematic diagram of proposed method.

3.2.1 Design of the holographic attenuating mirror

In the actual practices, HOE recording material has a grating detuning effect, which comes from the dimensional shrinkage induced by the chemical reactions during the holographic recording procedure [81, 82]. As a result, the Bragg condition for volume hologram is mismatched and the recorded information cannot be readout completely. Since the proposed method requires a uniform intensity and a uniform diffraction direction for the different diffraction orders, the grating detuning effect is an essential factor to be considered. The grating detuning effect caused by shrinkage of the material is illustrated as Fig. 3.6. In this chapter, the *v* and *u* stand for the thickness and transverse directions of the holographic material, respectively.

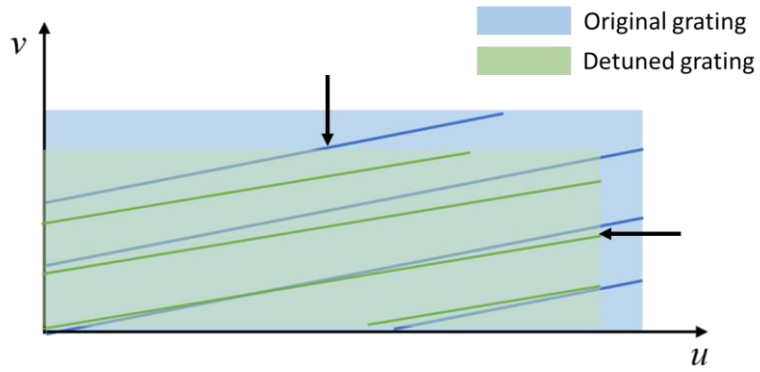

Figure 3.6 Grating detuning effect caused by dimensional shrinkage.

This work also adopts reflection type holograms. Wave vectors $\mathbf{k}_s$, $\mathbf{k}_r$, and $\mathbf{k}_g$ represent the signal, reference, grating vector; their corresponding

vectors after the shrinkage effect are denoted as $\mathbf{k_s}'$, $\mathbf{k_r}'$, and $\mathbf{k_g}'$, respectively, and their relation in vector space diagram is shown as Fig. 3.7.

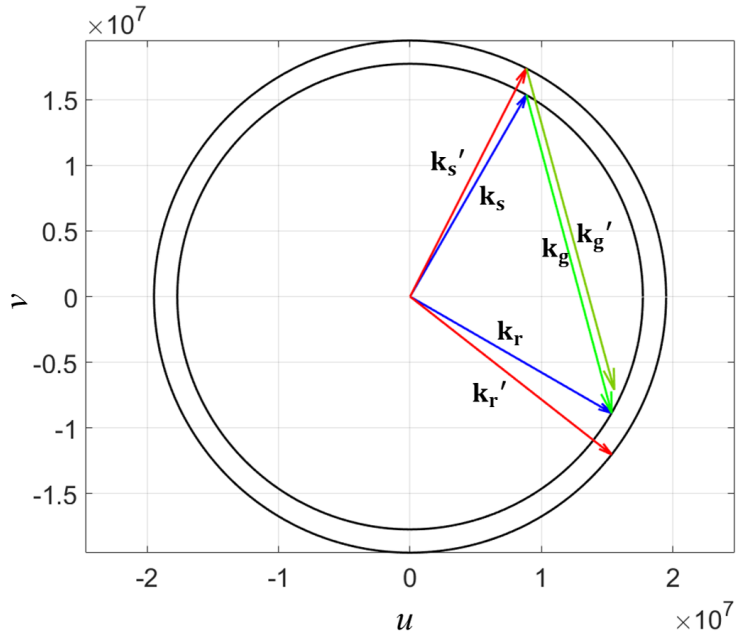

Figure 3.7 Vector space diagram for original grating and detuned grating cases.

According to Bragg's condition, the recorded grating vector $\mathbf{k_g}$ is given by

$$\mathbf{k_g} = \mathbf{k_s} + \mathbf{k_r}, \tag{3.1}$$

where $\mathbf{k_s}$ and $\mathbf{k_r}$ are the wave vectors of signal and reference waves inside the medium.

The outside signal and reference waves are incident to the medium with the angles θ_s and θ_r, respectively. θ_s and θ_r are the angles of those waves

after being refracted in the medium, which can be calculated by Snell's law: $\theta_{r\cdot in}=\sin^{-1}[\sin(\theta_r)/\rho]$ and $\theta_{s\cdot in}=\sin^{-1}[\sin(\theta_s)/\rho]$. n is the refractive index of the recording material. Since shrinkage effect occurs after HOE curing process, the recorded grating vector $\mathbf{k_g}$ is changed to $\mathbf{k'_g}$, which is given by Eq. (3.2).

$$\mathbf{k}'_{\mathrm{g}} = \hat{u}\left\{\frac{1}{1+\alpha_u}\left[|\mathbf{k_s}|\sin(\theta_s)-|\mathbf{k_r}|\sin(\theta_r)\right]\right\}+\hat{v}\left\{\frac{1}{1+\alpha_v}\left[|\mathbf{k_s}|\cos(\theta_s)+|\mathbf{k_s}|\cos(\theta_r)\right]\right\}, \tag{3.2}$$

where α_u and α_v are the shrinkage coefficients of the material along u and v axes, respectively. Due to the shrinkage effect, detuned grating vector $\mathbf{k'_g}$ induces phase mismatching when a probe wave, which is identical to the reference wave in the recording process, is illuminated to the HOE. Due to the grating detuning effect, the angles of probe and reconstruction waves to generate maximum diffraction efficiency are deviated from those of original ones. In order to get the Bragg-matching condition, the amount of the phase mismatching should be zero. In the actual display process, the directions of probe wave and reconstructed wave have been specified, which means the grating formation has been determined. Thus, the pre-compensated reference and signal waves can be determined experimentally. The recorded gratings should be detuned to match the desired ones after the curing process. There are several ways to compensate the grating vector such as angular deviation method and wavelength deviation method. We can flexibly use any one in the specific case if the formation of the desired gratings is specified.

As shown in Fig. 3.8, HOE_1, HOE_2, and HOE_3 are designed to align -1^{st}, 0^{th}, and $+1^{st}$ diffraction orders of the SLM, respectively. Mirror 1 (M_1) and mirror 2 (M_2) enable us to produce reference and signal waves by

appropriately adjusting the positions and angles. The reference waves with the angles θ_{r1}, θ_{r2}, θ_{r3}, and signal waves with the angles θ_{s1}, θ_{s2}, θ_{s3} are used for recording HOE_1, HOE_2, HOE_3, respectively. One of the key advantages of HOE is the adjustable diffraction efficiency, which follows the dosage used in the recording process. In order to keep the uniform intensity of the guided order terms, the exposure energy for recording each HOE should be handled according to the energy ratio between different diffraction orders of the SLM.

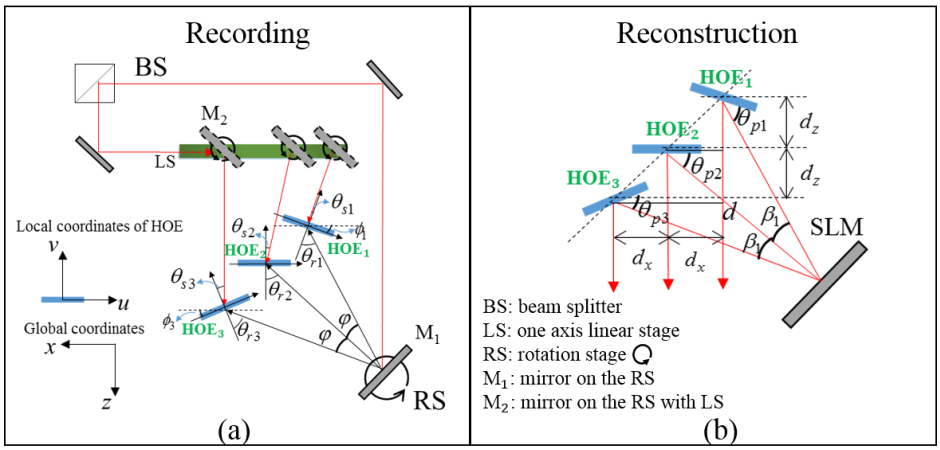

Figure 3.8 Schematic of the (a) recording and (b) reconstruction processes.

To control the diffraction efficiency ratio correctly, the energy ratio between the different diffraction orders of an SLM should be investigated. The SLM with periodic pixelated structure can be regarded as a set of square gratings. In a single period, the formula for one dimensional amplitude transmittance function of the SLM is given by Eq. (3.3)

$$t(x)=\begin{cases} C, & |x|<a/2 \\ 0, & a/2<|x|<p/2, \end{cases} \tag{3.3}$$

where a is size of the pixel aperture, p is pixel pitch of the SLM, and C is a constant. The square grating can be regarded as superposition of a series of sinusoidal gratings with different spatial frequencies. Let us denote $f_1=1/p$ as the fundamental frequency which provides the basic shape of the square grating. Then, coefficient of the Fourier series, which determines energy of the diffraction orders, is given by

$$\begin{aligned} T_n &= \frac{1}{p}\int_{-a/2}^{a/2} A\cdot\exp\left(-j2\pi f_n x\right)dx \\ &= \frac{A\cdot a\sin\left(\pi f_n a\right)}{\pi f_n a}, \end{aligned} \tag{3.4}$$

where f_n denotes the frequency of n-th wave, which is an integer multiple of the fundamental frequency. When a plane wave is incident to a single sinusoidal amplitude grating having the spatial frequency f_n, two diffraction orders with angles $\pm\beta_n=\sin^{-1}(\pm\lambda f_n)$ are generated, respectively. It means that high-order diffractions of an SLM are the terms of the Fourier series carrying different spatial frequencies. The intensities of the high-order components are also determined by the spatial frequencies and coefficients of the Fourier series expansions. Besides the diffraction on an individual pixel, the phase difference, which is induced by the interference among N pixels should also be considered. According to Eq. (3.4), the intensity distribution of the high-order diffraction beams can be calculated by

$$I_n = \left\{ \frac{\sin\left[\pi a \sin\left(\left| \pm\beta_n \right| \right) / \lambda \right]}{\pi a \sin\left(\left| \pm\beta_n \right| \right) / \lambda} \right\}^2 \left\{ \frac{\sin\left[N\pi d \sin\left(\left| \pm\beta_n \right| \right) / \lambda \right]}{N \sin\left[\pi d \sin\left(\left| \pm\beta_n \right| \right) / \lambda \right]} \right\}^2 . \quad (3.5)$$

In this work, the dosage for recording the HOE_1 and the HOE_3 reaches saturation level, and less dosage, which depends on the energy ratio between the adopted order terms, is used for recording the HOE_2.

In the reconstruction process, the direction of the reconstructed waves are specified to the same direction. In this case, the size of the reconstructed beam is determined by the angles of the probe wave and reconstructed wave of the HOE. In order to obtain a uniform size of the three diffraction order images, three HOEs are positioned according to the propagation directions of the three-order terms. If θ_{r2} is given, tilting angles of the HOE_1 and the HOE_3 can be calculated as

$$\begin{aligned} \phi_1 &= \tan^{-1}\left(\frac{\sin\left(\theta_{r2} + \beta_1 \right) - \cos\theta_{r2}}{\cos\left(\theta_{r2} + \varphi \right)} \right) \\ \phi_3 &= \tan^{-1}\left(\frac{\cos\theta_2 - \sin\left(\theta_{r2} - \beta_1 \right)}{\cos\left(\theta_{r2} - \varphi \right)} \right). \end{aligned} \quad (3.6)$$

For convenience of the alignment in the display process, HOE_2 is set to be parallel with x axis and θ_{p2} is specified as 45°. Thus, d_x and d_z indicated in Fig. 3.8 (b) are equal to each other. The distance between the centers of the SLM and the HOE_2 is given by $d=(d_x/\cos\theta_p)/\tan\varphi$, thus the positions of the HOEs for the reconstruction process can be determined.

The three different diffraction orders of the SLM are located at difference depth planes because of the path length difference d_z. Therefore, a

set of relay lenses having different focal lengths are required for imaging them at the same depth plane with the same size.

3.2.2 System implementation and experiment results

Figure 3.9 shows the dosage curve of the photopolymer. The diffraction efficiency were saturated when the dosage is over 10 mJ/cm^2 in this photopolymer (different photopolymer to the one used in the previous Chapter 2). According to Eq. (3.5) and the SLM specifications, the energy ratio between the $\pm 1^{st}$ and 0^{th} order diffraction beams is calculated as ~0.37. As shown in Fig. 3.19, the exposure energies for recording the HOE_1 and HOE_3 are marked in red circle; and the blue one is for HOE_2. The exposure energies for recording HOE_1 and HOE_3 reached at saturation level, so that they are able to provide a uniform diffraction efficiency.

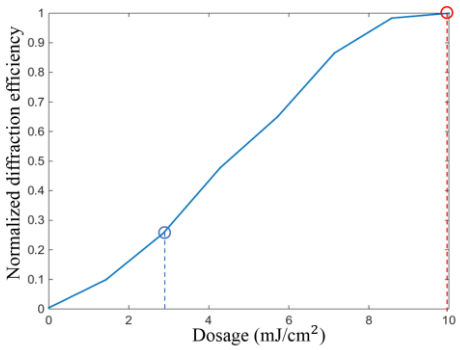

Figure 3.9 Diffraction efficiency according to exposure energy.

In order to get Bragg-matching condition, the angles of the reference and signal waves were pre-compensated. In the actual HOE recording

experiment, the actually used angles of reference and signal waves were as follows: θ_{r1}=49.8°, θ_{r2}=50.3°, θ_{r3}=51°, and θ_{s1}=6°, θ_{s2}=3.5°, θ_{s3}=4°; the tilting angle of the HOE_1 and HOE_3 were $\phi_1=\phi_3$=4.3°.

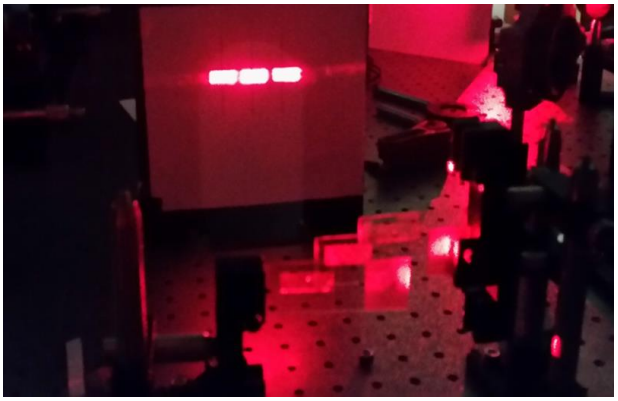

Figure 3.10 Aligned three diffraction orders by the HOEs.

In the reconstruction process, the intervals of the adjacent HOEs, in *x* and *z* axes were both d_x=25.4 mm, thus the distance from the center of SLM to that of the HOE_2 was 461.5 mm, and θ_{p1}, θ_{p2}, and θ_{p3}, were all 45°. The horizontal size of the SLM was 16.32 mm, then the images size after being guided by the corresponding HOEs were all w'=23.08 mm. Figure 3.11 shows the guided three diffraction orders of the SLM using the designed HOEs. The experiment verifies that the HOE is possible to guide them to an identical direction (i.e. *z* axis) with a uniform intensity.

An experiment was carried out for investigating the aberration of the reconstructed hologram. A normal Fresnel zone plate (FZP) propagated to the HOE by θ_p=45°. A screen was placed on an optical rail to adjust the

position along z axis. Figure 3.11 shows the experimental configuration, setup and the captured reconstruction images at different depths.

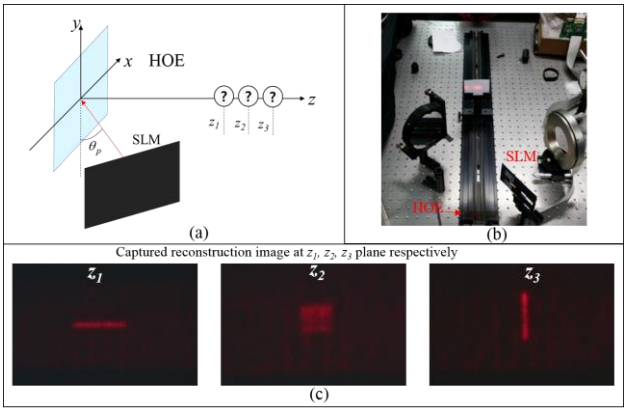

Figure 3.11 Measurement of FZP aberration. (a) Configuration and (b) the experimental setup. (c) Captured reconstruction images.

Figure 3.11(c) shows that the reconstructed image is merely focused in the vertical direction at the depth plane z_1, which was the original focal plane of the FZP. Since, the FZP was stretched in the horizontal direction by use of the HOE, the focal length along the vertical direction maintained unchanged. As shown in Fig. 3.11(c), the wavefront was a diverging spherical wave along the vertical direction and a converging spherical wave along the horizontal direction within the range from z_1 to z_3. It means that the focal length of the FZP in the horizontal direction was extended. The aberration compensation method mentioned in Chapter 2 is used, so that a target spot can be focused at the correct depth plane. Figure 3.12 shows the experimental results for verifying the compensation algorithm.

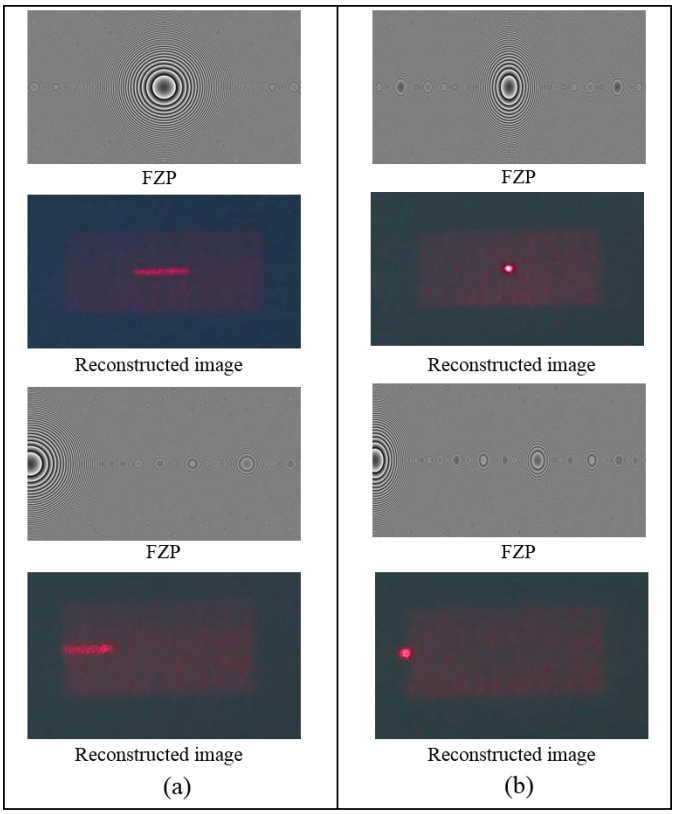

Figure 3.12 Comparison of the reconstructed holograms: (a) without using the compensation method and (b) using the compensation method.

Figure 3.13 shows the configuration of the proposed holographic display system. In order to remove the gap between adjacent order terms in the display process, the relay lenses L_1 and L_2 were designed as square shape. The three diffraction order images can be regarded as three virtual SLMs located at different depths along *z* axis. Thus, a set of relay lenses (L_1), which have the different focal lengths, were used for imaging them at the same

depth plane and with the same magnification. The parameters of the relay lenses and the virtual SLMs are listed in Table 3.2.

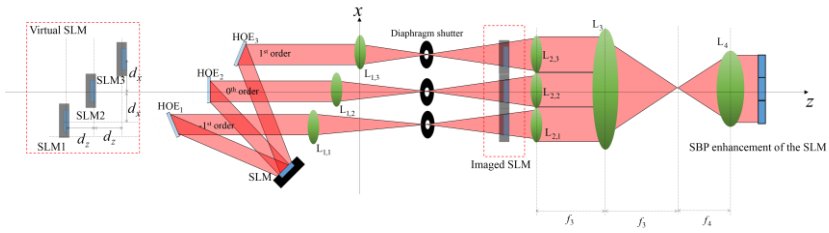

Figure 3.13 Configuration of proposed holographic display system.

Table 3.2 Parameters of the relay lenses and virtual SLMs

Relay lenses				Virtual SLMs	
Item	Center coordinates in *x*-*z* plane (mm)	Width(w)/Diameter(d) (mm^2)	Focal length (mm)	Item	Center coordinates in *x*-*z* plane (mm)
$L_{1,1}$	(-25.4,-23.8)	25.4(w)	341	SLM_1	(-25.4,-705.8)
$L_{1,2}$	(0,-10.4)	25.4(w)	335	SLM_2	(0,-680.4)
$L_{1,3}$	(25.4,0)	25.4(w)	328	SLM_3	(25.4,-655)
$L_{2,1}$	(-25.4,691)	25.4(w)	367		
$L_{2,2}$	(0,691)	25.4(w)	367		
$L_{2,1}$	(25.4,691)	25.4(w)	367		
L_3	(0,991)	127(d)	300		
L_4	(0,1491)	50.8(d)	200		

In order to increase SBP, they are displayed using a temporal-multiplexing technic. In the system, three electro-shutters (Thorlabs Co.,

SHB05T high speed shutter) whose maximum operation speed was 15 Hz, were synchronized with the corresponding diffraction order, and an Arduino UNO R3 micro controller board was used for sending the signal to the shutters. According to the frequency specified at the output port of the control board, it sent on/off signals to the shutters and the computer simultaneously. OpenGL and OpenCV library were used for enhancing the display speed of the holograms. The size of the eyebox size and FOV the display were 50.8 mm and 4.3°. The FOV and eyebox size can be adjusted to optimization values for near-eye holography. As a result, the display system can provide 30° FOV and 6mm eyebox size. Figure 3.14 shows the benchtop of the proposed holographic display.

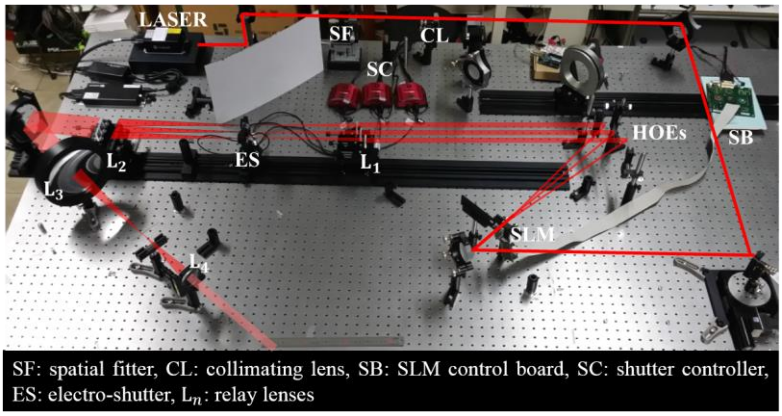

Figure 3.14 Experimental setup of the proposed holographic display system.

In order to confirm the advantage of the SBP enhancement, the apertures of the three diffraction orders were released sequentially as shown in Fig. 3.15. By utilizing a temporal-multiplexing technic, holograms of

letters “S”, “N”, and “U” were modulated by -1st, 0th, and 1st diffraction orders of the SLM, respectively. The result shows that it is able to obtain three-fold increase in SBP of a single SLM.

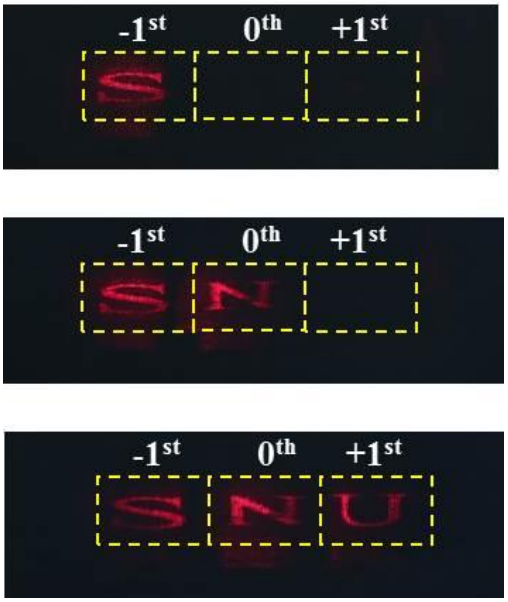

Figure 3.15 Experimental results of the reconstructed holograms by the holographic display with increased SBP.

3.3 Polarization selective holography

3.3.1 Principle of polarization selective holography

For a liquid crystal (LC) based SLM, the amplitude or phase of input lights is modulated by sandwiching the SLM between a set of polarizers in specific states. It means that by adjusting an optical system, which consists of phase retardation and polarization optical elements, one can get different responses to the input light. Since the SLM has a pixelated structure, high-order diffractions, which contain the same information to each other, inherently occur in the holographic display. Thus, if we set different optical systems at the path of the different diffraction order paths, a single SLM can also provide different functions *f* and *g*. The configuration of the proposed method is depicted in Fig. 3.16.

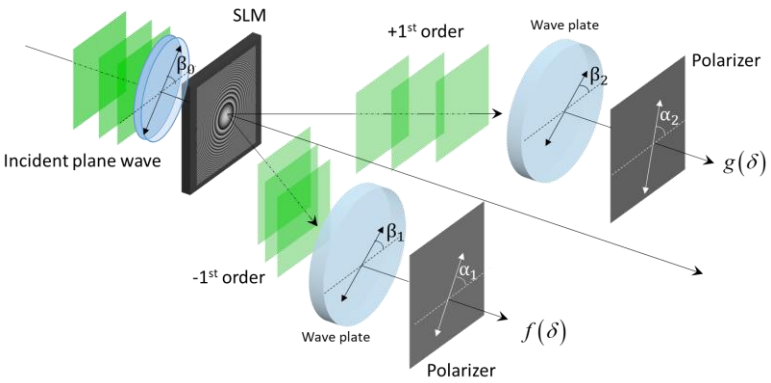

Figure 3.16 Concept of the polarization selective holography.

As shown in Fig. 3.16, polarized lights illuminate an SLM, and a wave

plate whose fast axis angle is β_0 and wave retardation is γ_0 is placed in front of the SLM. In the paths of the +1st and -1st diffraction order of the SLM, linear polarizers with the axis direction α_1 and α_1; wave retarders with the fast axis angle β_1, β_2 and phase retardation γ_1, γ_2 are placed as shown in Fig. 3.16. Thus, the output wave field can be calculated by Jones Matrix [71, 83].

$$\begin{aligned} \mathrm{v}_{\mathrm{out}} = & \begin{pmatrix} \cos^2\alpha & \frac{\sin 2\alpha}{2} \\ \frac{\sin 2\alpha}{2} & \sin^2\alpha \end{pmatrix} \begin{pmatrix} \cos\frac{\gamma}{2} + i\cos 2\beta \sin\frac{\gamma}{2} & i\sin\frac{\gamma}{2}\sin 2\beta \\ i\sin\frac{\gamma}{2}\sin 2\beta & \cos\frac{\gamma}{2} - i\cos 2\beta\sin\frac{\gamma}{2} \end{pmatrix} \\ & \begin{pmatrix} \frac{e^{\delta i}+1}{2} & \frac{1-e^{\delta i}}{2} \\ \frac{1-e^{\delta i}}{2} & \frac{e^{\delta i}+1}{2} \end{pmatrix} \begin{pmatrix} \cos\frac{\gamma_0}{2} + i\cos 2\beta_0 \sin\frac{\gamma_0}{2} & i\sin\frac{\gamma_0}{2}\sin 2\beta_0 \\ i\sin\frac{\gamma_0}{2}\sin 2\beta_0 & \cos\frac{\gamma_0}{2} - i\cos 2\beta_0\sin\frac{\gamma_0}{2} \end{pmatrix} \mathrm{v}_{\mathrm{in}} \end{aligned} \tag{3.7}$$

Third matrix is the Jones Matrix of an SLM with 45° alignment direction of LC, where δ is the phase retardation related to voltage applied. Thus, the amplitude A and phase φ of the output optical field are given by

$$\begin{aligned} A &= \left| \begin{bmatrix} \cos\alpha & \sin\alpha \end{bmatrix} \cdot \mathrm{v}_{\mathrm{out}} \right| \\ \varphi &= \angle\left(\begin{bmatrix} \cos\alpha & \sin\alpha \end{bmatrix} \cdot \mathrm{v}_{\mathrm{out}} \right) \end{aligned} \tag{3.8}$$

As a result, if we can find an optimized condition for the 8 parameters (γ_0, β_0, γ_1, β_1, α_1, γ_2, β_2, α_2), the optical systems can modulate different optical waves: $A_1(x,y)$ and $A_2(x,y)$, according to the corresponding mode. We assume there is a coordinate system whose horizontal and vertical axes are represented by A_1 and A_2, respectively. Thus, the coordinate of a point on the A_1-A_2 plane represents that a set of intensity combination for the two amplitude modulation set. By changing the LC retardation δ from 0 to π (i.e.

gray level: 0-255), I can draw an amplitude combination map (ACM) on the A_1-A_2 plane. For an 8 bit gray level SLM, the point number of ACM is 256 and the ideal distribution is shown in Fig. 3.17. In this case, two holograms quantized by 4 bit can be perfectly encoded for the two modes, respectively.

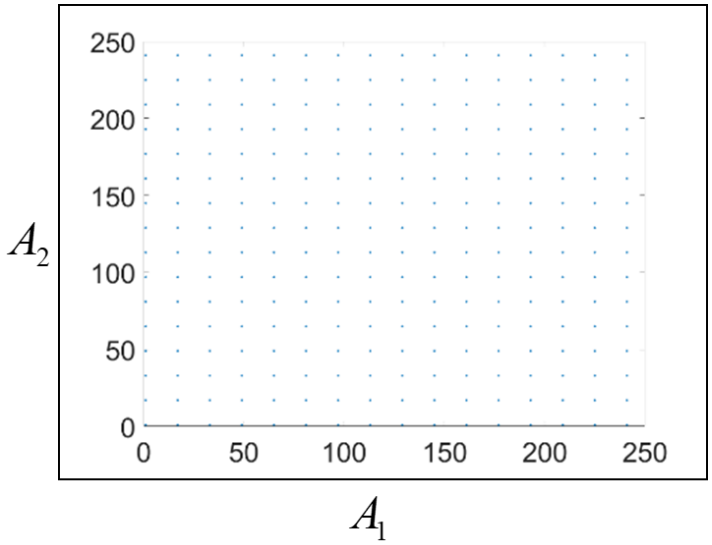

Figure 3.17 The ideal case of ACM for an 8 bit gray level SLM.

If we have two holograms for the modes, the hologram combination map (HCM) can also be represented on the A_1-A_2 plane and their coordinate set on the plane is given by $[A_1(x,y), A_2(x,y)]$.

The principle to encode the hologram using amplitude modulation is explained as follows. An optical wave field is generally characterized by two independent variables at a given point, i.e., the phase and amplitude. Theoretically, complex SLM can generate perfect optical wave fields with controlled amplitudes and phases. However, in practices, such a complex

SLM has not yet been reported and most available SLMs are designed to be in the form of amplitude-only or phase-only SLMs with only one degree of freedom.

In the proposed method, I adopted a single-sideband technic to encode hologram for an amplitude-only SLM [65-67]. Figure 3.18 shows a 4*f* optical system used in the single-sideband technic. $g(x,y)$ represents a desired optical wave field which is at the image plane and corresponding Fourier transform is denoted by $G(u,v)$. To separate the signal and conjugate term, $G(u,v)$ is shifted by carrier frequencies amount Δu and Δv along the horizontal and vertical directions, respectively. Furthermore, the complex amplitude on the amplitude-only SLM is real value, thus the distribution $G_s(u,v)$ at the Fourier plane has Hermitian symmetry property as $G_s(u,v)= G_s^*(-u,-v)$ and it is given by

$$G_s(u,v) = G(u-\Delta u, v-\Delta v) + G^*(-u+\Delta u, v+\Delta v). \qquad (3.9)$$

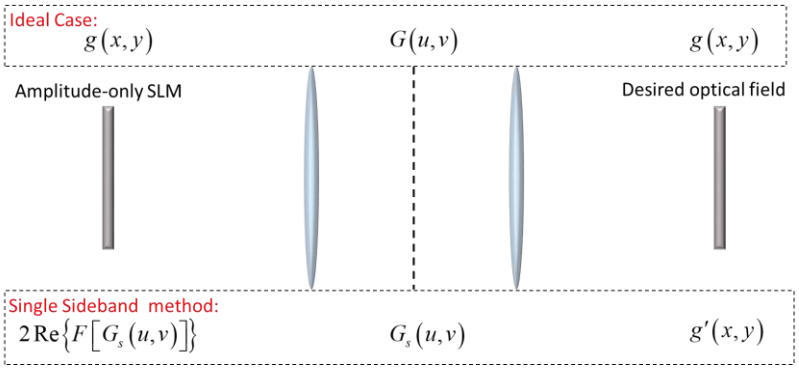

Figure 3.18 Single-sideband encoding method for an amplitude-only SLM.

Thus, we can get a real-valued function to be encoded on the amplitude-

only SLM, which is given by 2Re{$F[G_s(u,v)]$}. Note that, as the gray level values represented by the amplitude-only SLM are positive, a bias component $b(x,y)$ is added to the encoded field to shift to nonnegative. Summation of bias and un-diffracted DC components generates a delta function at the center of the Fourier plane. Finally, the reconstructed optical field is given by

$$g'(x,y) = g(x,y)\exp\left[-j2\pi\left(u\cdot\Delta u + v\cdot\Delta v\right)\right]. \qquad (3.10)$$

An exponential term that is multiplied to $g(x,y)$, yields bandwidth shifting which changes propagation direction of the filed in the image plane. As shown in Fig. 3.16, masking the conjugate and the DC terms limits at least half of the original bandwidth. The pixel pitch of the SLM is defined as p, thus the expressible bandwidth is given by $1/2p$. As a result, the desired field $g(x,y)$ propagates with reduced diffraction angle $\theta \leq \sin^{-1}(\lambda/2p)$.

If the HCM, which is the hologram for amplitude-only SLM, is mapped to ACM, two different holograms can be generated independently. Thus, how to find an optimized ACM is the key issue in the proposed method.

3.3.2 Amplitude combination map optimization using genetic algorithm

We solve the optimization problem using genetic algorithm and it is explained in this section. Figure 3.19 shows the flow chart of the genetic algorithm [84, 85]. In the generation stage, the initial population P_0 with a population size n is generated. The population consists of chromosome c_i having 8 parameters $c(\gamma_0, \beta_0, \gamma_1, \beta_1, \alpha_1, \gamma_2, \beta_2, \alpha_2)$ which are called genes. In

the evolution stage, chromosomes having the highest fitness values are determined by solving their fitness function, which is the most important factor for determining the performance of the GA.

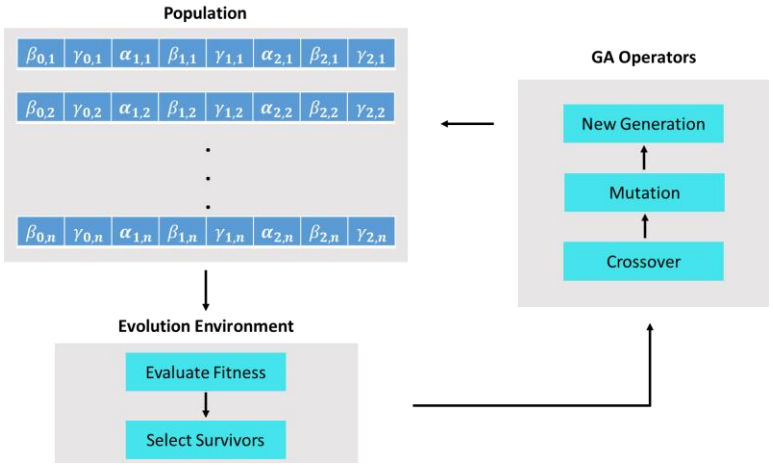

Figure 3.19 Flow chart of the genetic algorithm.

In the evolution stage, the solution of the optimization problem converges through a crossover and mutation processes. Several pairs of chromosomes with highest performance are specified as parents. The crossover process between the parents is carried out by randomly mixing their genes i.e. 8 parameters. The reproduced new chromosomes is used to search the local optima again. Assume that the performance of the first generation chromosomes are not good enough, it is difficult to get a global optima just using the crossover process. Thus, a mutation process is essential in every generation, so that it makes small variations of the present solution and searches the optimum solution randomly.

As a result, optimized variables set is obtained as: β_0=11.7°, γ_0=165°, α_1=336°, β_1=161°, γ_1=12°; α_2=147°, β_2=204°, γ_2=58°.

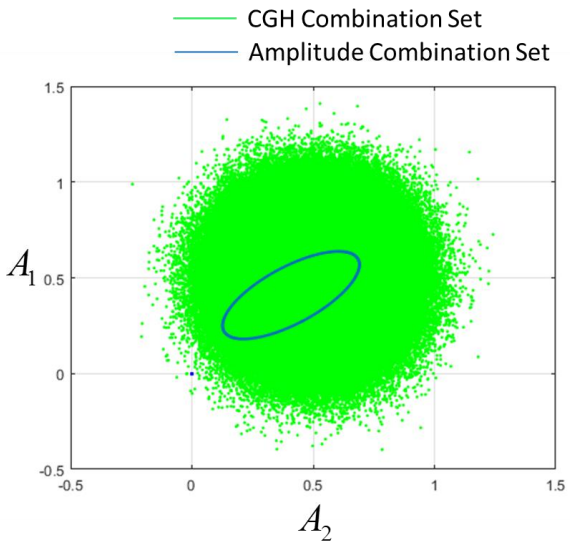

Figure 3.20 ACM and HCM distribution at A_1-A_2 plane.

As mentioned in the previous section, the distribution of the more complex or wider ACM is better. The blue line in Fig. 3.20 is the most widely distributed map. The CGH to be displayed on an SLM is obtained by mapping the HCM (red dots in Fig. 3.20) to the ACM (green dots in Fig. 3.20). In the mapping process, each point of the HCM finds the closest point on the ACM, and the searched value of ACM is encoded to the SLM pixel.

3.3.3 Simulation and experimental results

Figure 3.21 shows the simulation result using the proposed method. The mapped CGH reconstructs different images in accordance with each modulation mode (+1st diffraction order & -1st diffraction order). The object used in the simulation and the experiment is a letter “A” and a letter “B”.

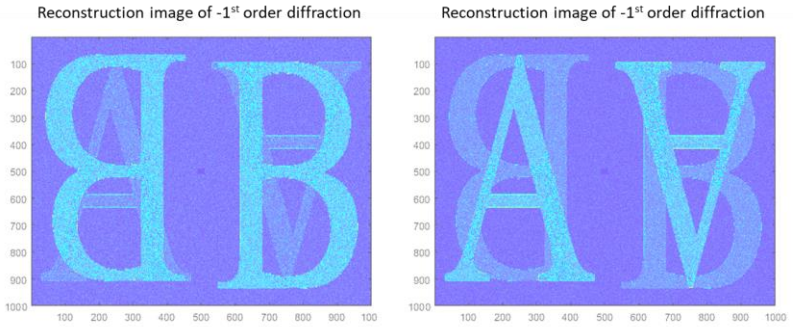

Figure 3.21 Simulation results using polarization selective holography.

As shown in the result, the left figure has more crosstalk. This is because the obtained ACM is not symmetric in the horizontal and vertical axis as shown in Fig. 3.20, which means the ACM can modulate more values for -1st diffraction order than 1st order diffraction mode.

Figure 3.22 shows the experimental result using the proposed method. Electronically controllable full-wave liquid crystal variable retarder is used to precisely adjust the wave retardation and the fast axis angle according to the optimized variables; and a polarizer with a rotation mount is used to adjust the polarizer angle.

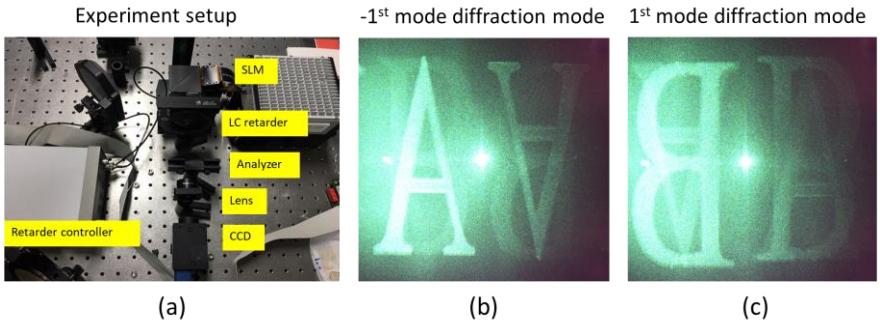

Figure 3.22 (a) Experimental setup. Reconstruction images: (b) -1^{st} diffraction mode, (c) $+1^{st}$ diffraction mode.

The experimental results also show crosstalk in the two modes. The reasons are as follows: 1. the performance of the fitness function used in the genetic algorithm is not good enough to find a perfect optimized solution set. 2. LC retarder is not controlled correctly enough, because I did not have the lookup table of the retarder in the 532 nm wavelength which is the light source used in the experiment.

3.4 Synthesis of computer generated spherical hologram

Majority of hologram computation methods are introduced based on planar hologram architecture. Comparing to the planar hologram, a curved hologram has an important advantage in saving required sampling number. In this section, I introduce the proposed spherical hologram computation method of real objects.

3.4.1 Spatial spectral bandwidth of spherical hologram

CGH calculation requires the full 3D information of the objects. For each object point, the light field distribution at any positions in the space is defined as below,

$$H(x, y, z) = \frac{A_i \exp(jkd_i)}{d_i}, \tag{3.11}$$

where $k=2\pi/\lambda$ is the wave number, λ is the wavelength, A_i is the intensity of the object point, and d_i is the length of the vector pointing from the object point $P_i(x_i, y_i, z_i)$ to the recording point $P(x, y, z)$, which is given by

$$d_i = \sqrt{(x-x_i)^2 + (y-y_i)^2 + (z-z_i)^2}. \tag{3.12}$$

In order to calculate the light distribution on the spherical surface, it is advantageous to use the spherical coordinates system, thus the diffraction field of the spherical hologram is given by

$$H_r(\theta,\varphi)=\frac{A_i\exp\left\{jk\left[\begin{array}{l}\left(r\sin\theta\cos\varphi-x_i\right)^2+\\ \left(r\sin\theta\sin\varphi-y_i\right)^2+\left(r\cos\theta-z_i\right)^2\end{array}\right]^{1/2}\right\}}{\left[\begin{array}{l}\left(r\sin\theta\cos\varphi-x_i\right)^2\\ +\left(r\sin\theta\sin\varphi-y_i\right)^2+\left(r\cos\theta-z_i\right)^2\end{array}\right]^{1/2}},$$

where radius of the hologram is denoted as r, the latitudinal axis is defined as θ and the azimuthal axis is defined as φ. Figure 3.33 shows one example of the calculated optical field when a point object is located at (x_i, y_i, z_i)=(0, 0, 0.1m), where λ=532 nm and r=1 m.

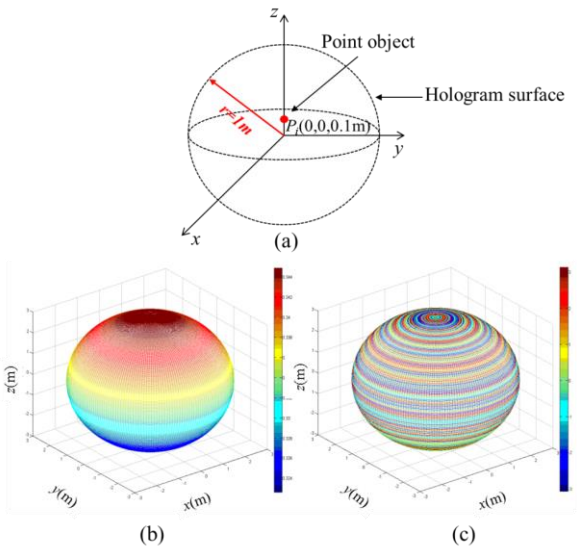

Figure 3.23 (a) Position of the object point and the hologram surface. (b) Amplitude and (c) phase distribution of the spherical hologram.

In order to compute a spherical hologram, it is necessary to analyze the spatial spectral bandwidth. The sampling theorem should be satisfied in both

the latitudinal and azimuthal directions. The local spatial frequency pair ($f_{L\theta}$, $f_{L\varphi}$) of the phase of the spherical hologram $H_r(\theta, \varphi)$ is given by [52]

$$\begin{aligned} f_{L\theta} &= \frac{1}{2\pi}\frac{\partial}{\partial\theta}(kd_i), \\ f_{L\varphi} &= \frac{1}{2\pi}\frac{\partial}{\partial\varphi}(kd_i), \end{aligned} \tag{3.14}$$

which leads to

$$\begin{aligned} f_{L\theta} &= \frac{kr(x_i\cos\theta\cos\varphi + y_i\cos\theta\sin\varphi - z_i\sin\theta)}{2\pi\left[\left(r\sin\theta\cos\varphi - x_i\right)^2 + \left(r\sin\theta\sin\varphi - y_i\right)^2 + \left(r\cos\theta - z_i\right)^2\right]^{1/2}}, \\ f_{L\varphi} &= \frac{r\sin\theta(x_i\sin\varphi - y_i\cos\varphi)}{2\pi\left[\left(r\sin\theta\cos\varphi - x_i\right)^2 + \left(r\sin\theta\sin\varphi - y_i\right)^2 + \left(r\cos\theta - z_i\right)^2\right]^{1/2}}. \end{aligned} \tag{3.15}$$

Without loss of generality, the object point P_i is assumed to be located at $(x_i, y_i, z_i)=(r_o, 0, 0)$ as denoted in Fig. 3.24. Thus, the local frequencies corresponding to the point object can be written as

$$\begin{aligned} f_{L\theta} &= \frac{krr_o\cos\theta\cos\varphi}{2\pi\left(r^2 - 2rr_o\sin\theta\cos\varphi + r_o^2\right)^{1/2}}, \\ f_{L\varphi} &= \frac{krr_o\sin\theta\sin\varphi}{2\pi\left(r^2 - 2rr_o\sin\theta\cos\varphi + r_o^2\right)^{1/2}}. \end{aligned} \tag{3.16}$$

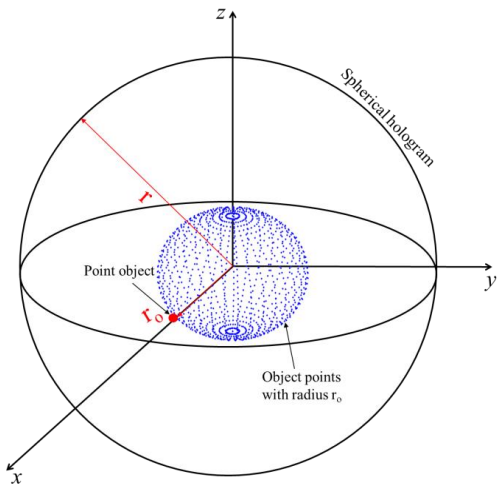

Figure 3.24 Object points with the same distance from coordinate origin.

According to Eq. (6), the maximum local spatial frequency $|f_{L\theta}|_{\max}$ appears at the position where $\theta=\sin^{-1}(r_o/r)$, $\varphi=0$ of the hologram surface, and is given by

$$|f_{L\theta}|_{\max}=\frac{kr_o}{2\pi}. \tag{3.17}$$

In the same way, $|f_{L\theta}|_{\max}$ is given by

$$|f_{L\varphi}|_{\max}=\frac{kr_o}{2\pi}. \tag{3.18}$$

For φ direction, the maximum local frequency $|f_{L\theta}|_{\max}$ appears at the position where $\theta=\pi/2$, $\varphi=\sin^{-1}(r_o/r)$ of the hologram surface. The results shown above indicate that the object point located farther from the coordinate origin requires higher local frequency for the spherical hologram. The minimum

number of hologram points to satisfy the Nyquist sampling theorem in each axis is given by

$$N_\theta = 2\pi \cdot \left| f_{L\theta} \right|_{\max} = kr_o, \\ N_\varphi = 4\pi \cdot \left| f_{L\varphi} \right|_{\max} = 2kr_o. \tag{3.19}$$

One of the key advantages of the spherical hologram is that the data amount for a given field of view is smaller than a planar hologram. Suppose a two-dimensional case where a point object is located at $P(x_i, y_i) = P(d', 0)$ to as shown in Fig. 3.25.

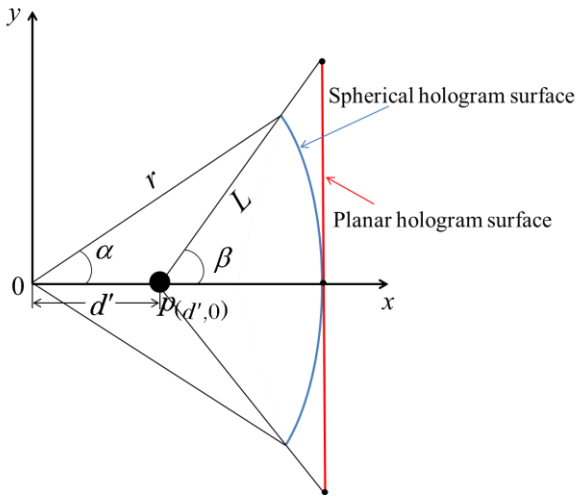

Figure 3.25 Spherical and planar hologram for optical field of the same FOV.

For a 2β FOV, the maximum spatial frequency is given by $\left| f_{L\theta} \right|_{\max} = kd'/2\pi$ for a spherical hologram, and $\left| f_{Ly} \right|_{\max} = k\sin\beta/2\pi$ for a planar hologram. Therefore, the number of required samples to represent the optical field is much larger in planar hologram as depicted in Fig. 3.26.

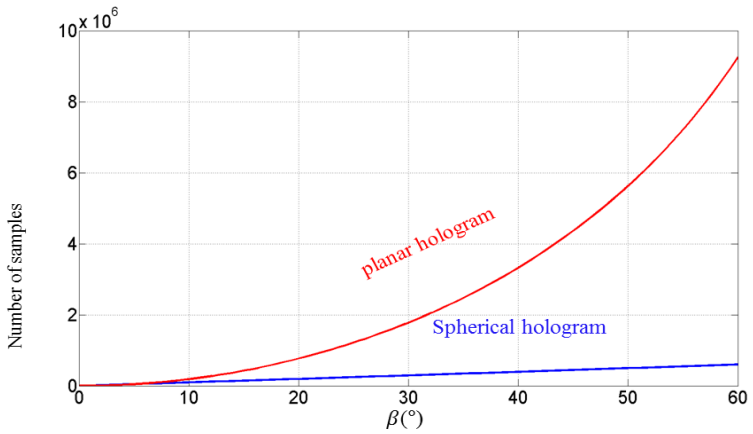

Figure 3.26 Required number of samples for the spherical and the planar hologram. d'= 0.18 m, r=1 m.

The result reveals that using spherical hologram can significantly decrease the data amount than using planar hologram in case of large FOV.

3.4.2 Spherical hologram calculation of real objects

In spherical hologram, the 3D information acquisition of the real object is a key element. In order to extract 360° depth information of a real object, I captured a real object by placing depth camera in front, rear, left, and right sides around it. Figure 3.27 shows the four sets of the point cloud, which are extracted by the depth camera in corresponding directions.

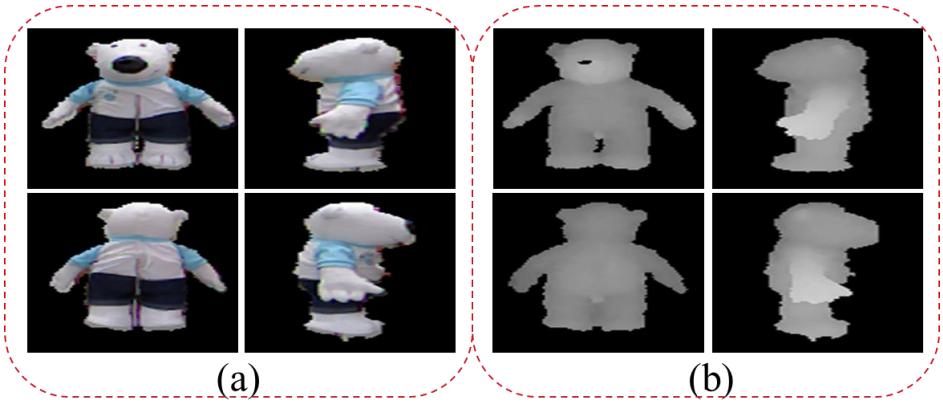

Figure 3.27 Extracted depth maps of the object in multiple directions. (a) Color images of the object, (b) corresponding depth map images.

The obtained point cloud sets need to be brought into a common coordinate system, since each depth map is captured in its own coordinate system. In our proposed method, the point cloud registration (PCR) algorithm is used. The PCR process consists of two steps, i.e. rotating and shifting as given by

$$\hat{P}_T = R \cdot \hat{P}_o + T, \tag{3.20}$$

where $\hat{P}_o$ the initial point cloud, $\hat{P}_T$ the registered point cloud, R rotation matrix, and T is the translation matrix. The rotation matrix R is given by

$$R = \begin{bmatrix} 1, & 0, & 0 \\ 0, & \cos\gamma_x, & -\sin\gamma_x \\ 0, & \sin\gamma_x, & \cos\gamma_x \end{bmatrix} \begin{bmatrix} \cos\gamma_y, & 0, & \sin\gamma_y \\ 0, & 1, & 0 \\ -\sin\gamma_y, & 0, & \cos\gamma_y \end{bmatrix} \begin{bmatrix} \cos\gamma_z, & -\sin\gamma_z, & 0 \\ \sin\gamma_z, & \cos\gamma_z, & 0 \\ 0, & 0, & 1 \end{bmatrix} \tag{3.21}$$

where rotation angles about x, y and z axes are denoted as γ_x, γ_y and γ_z, respectively. Since the depth camera is set to capture the object around z axis, γ_x, and γ_y are 0° in the proposed method. The point cloud, which is obtained from front side of the object, is specified as the reference model. Thus, the rotation angle γ_z of data obtained from right, rear, and left side of the object are 90°, 180°, and 270°, respectively. The original point cloud sets and the rotated ones are shown in Fig. 3.28

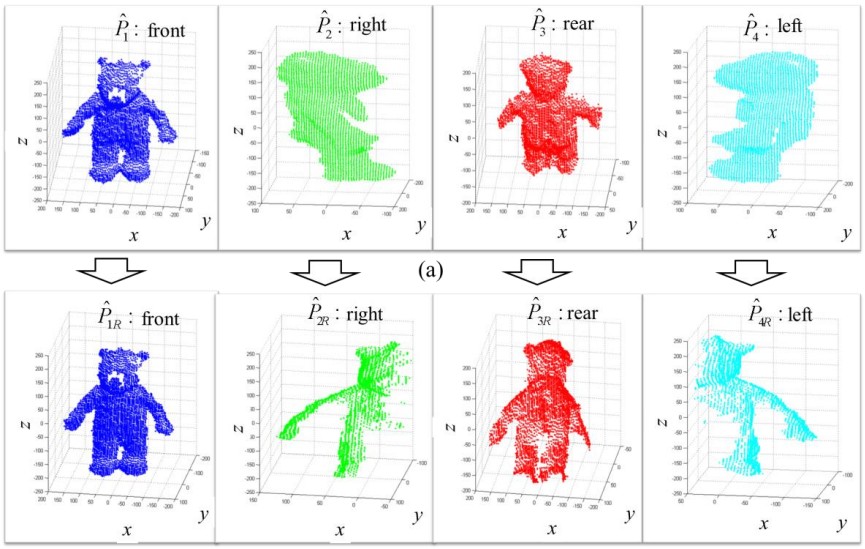

Figure 3.28 Rotation of the initial point cloud sets. (a) Initial point clouds and (b) rotated ones.

The rotated point cloud sets are denoted as $\hat{P}_{1R}$, $\hat{P}_{2R}$, $\hat{P}_{3R}$ and $\hat{P}_{4R}$, respectively. After rotation, the translation vector T_i for each point cloud $\hat{P}_{iR}$ is given by

$$
\begin{aligned}
T_1 &= [0,0,0] \\
T_2 &= \left[m_{1x} - m_{2x}, m_{1y} - m_{2y}, m_{1z} - m_{2z} \right] \\
T_3 &= \left[m_{1x} - m_{3x}, m_{1y} - m_{3y}, m_{1z} - m_{3z} \right] \\
T_4 &= \left[m_{1x} - m_{4x}, m_{1y} - m_{4y}, m_{1z} - m_{4z} \right],
\end{aligned}
\tag{3.22}
$$

where, m_{ix}, m_{iy} and m_{iz} denote maximum coordinate values of the rotated point cloud $\hat{P}_{iR}$ in x, y, and z axes. Finally, a 3D model $\hat{P}_T$ that contains 360° depth information can be obtained by

$$
\hat{P}_T = \hat{P}_{1R} \bigcup (\hat{P}_{2R} + T_2) \bigcup (\hat{P}_{3R} + T_3) \bigcup (\hat{P}_{4R} + T_4), \tag{3.23}
$$

where $\cup$ stands for union operation. Figure 3.29 shows the 3D model constructed by PCR.

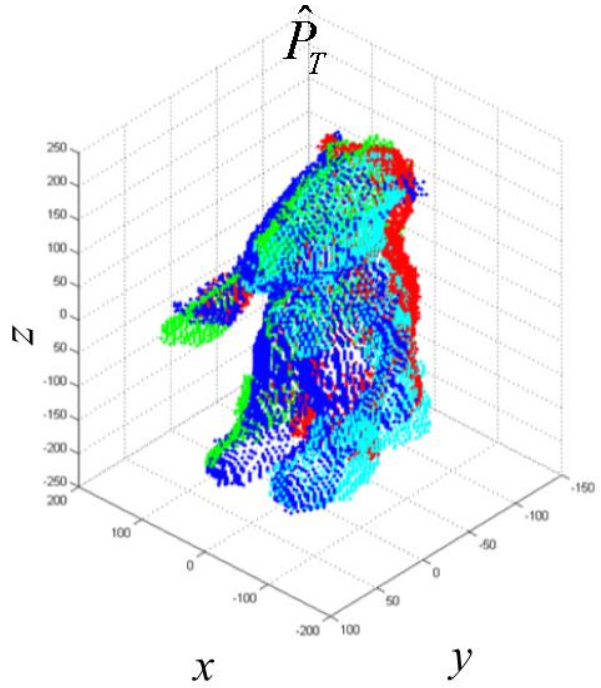

Figure 3.29 Acquired 3D model of the real object.

After registration, visible point set for a given viewpoint needs to be identified for correct occlusion effect. In our method, the HPR technique is used [49]. The HPR technique consists of two steps, i.e. inversion flipping and convex hull extraction. First, the object point cloud $\hat{P}_T$ is converted by spherical flipping function, which is expressed as

$$\hat{P}_f = \hat{P}_T + 2(r_f - \left\|\hat{P}_T\right\|)\frac{\hat{P}_T}{\left\|\hat{P}_T\right\|}, \tag{3.24}$$

where $\left\|\hat{P}_T\right\| = \left(\hat{P}_T \cdot \hat{P}_T\right)^{1/2}$ and r_f is the longest distance between the hologram point $H_r(\theta, \varphi)$ and the object point. By using Eq. (3.24), the object point cloud can be flipped as shown in Fig. 3.30.

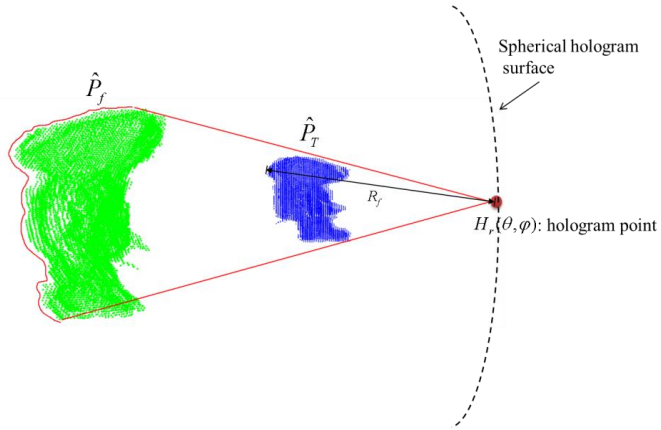

Figure 3.30 Spherical flipping of the 3D point cloud by Eq. (3.24). The object point cloud $\hat{P}_T$ and the flipped point cloud $\hat{P}_f$.

Step 2 is the process of extracting convex hull. Convex hull of the point set, which is marked in red line in Fig. 3.30, is the smallest convex set that contains the hologram point and the flipped point cloud. The selected convex hull points are visible to the given hologram point. Figure 3.31 shows the result of the HPR. The visible points set of the object at the hologram point $H_r(\theta, \varphi)$ is denoted as $\hat{P}_{(\theta,\varphi)}$.

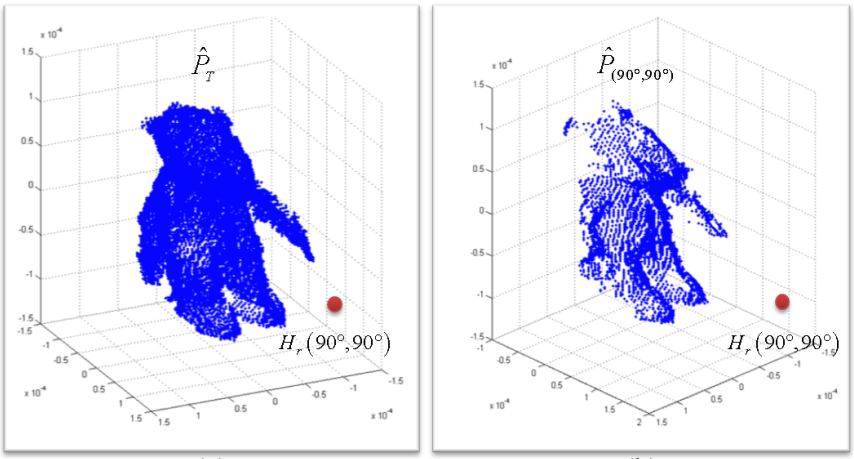

(a) (b)

Figure 3.31 (a) Entire points without HPR and (b) the visible point set processed by HPR at the hologram point H_r(90°, 90°).

In our proposed method, the visible object points are identified for each hologram point as illustrated in Fig. 3.32.

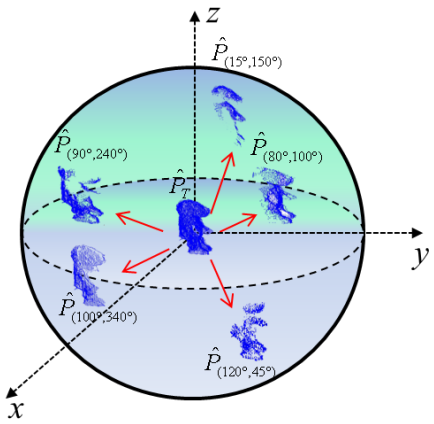

Figure 3.32 Visible point set for each hologram point.

Thus, a complex value of the hologram point is given by

$$H_r(\theta,\varphi)=\sum_{i=1}^{N}A_i\frac{\exp\left\{jk\left[\begin{array}{l}\left(r\sin\theta\cos\varphi-x_i\right)^2+\\\left(r\sin\theta\sin\varphi-y_i\right)^2+\left(r\cos\theta-z_i\right)^2\end{array}\right]^{1/2}\right\}}{\left[\begin{array}{l}\left(r\sin\theta\cos\varphi-x_i\right)^2+\\\left(r\sin\theta\sin\varphi-y_i\right)^2+\left(r\cos\theta-z_i\right)^2\end{array}\right]^{1/2}}. \tag{3.25}$$

where A_i is intensity of the *i-th* point of the visible point set $\hat{P}_{(\theta,\varphi)}$ and the Cartesian coordinates of the point is (x_i, y_i, z_i). This computation is performed repeatedly until the optical field values for all spherical hologram points are determined.

3.4.3 Simulation and experiment results

The proposed method is verified experimentally. First, I show the spherical holograms for a single object point. Figure 3.33 shows the amplitude and phase images when the object point is located at several different positions. The first row images are calculated in the case that the object point is located at (x_i, y_i, z_i)=(0, 0, 0.01 mm). Second, third and last rows are the amplitude and phase images when the point located at (x_i, y_i, z_i)=(0, 0.1 mm, 0), (x_i, y_i, z_i)=(0.1 mm, 0, 0), and (x_i, y_i, z_i)=(0.058 mm, 0.058 mm, 0.058 mm) with the r=10 mm, respectively. According to Eq. (3.19), the required number of samples in the spherical hologram is calculated as 1181(θ) ×2362(φ).

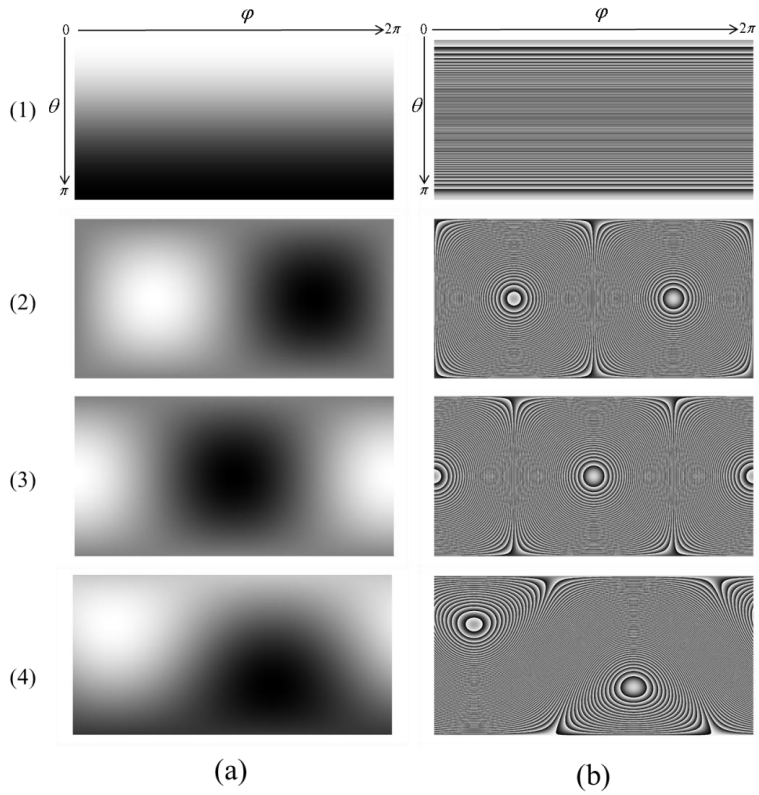

Figure 3.33 Spherical hologram generated by one point object. (a) Amplitude and (b) phase images

After confirming the spherical hologram generated by one light point source, the experiment of spherical hologram of real object is performed. In the experiment, KINECT sensor is used as the depth camera to extract object depth information. Recently Microsoft released a non-commercial KINECT software development kit (SDK) for Window 7. I use C# program language to run the KINECT SDK. The resolution of each depth map image obtained using KINECT is 320(V)×240(H). The acquired 3D model of the real object in Fig. 3.34 is composed of 14531 points while size of the object is limited in

the range from -1.4 mm to +1.4 mm in each x, y and z axis. In the experiment, the radius r of the spherical hologram is set to 95.7 mm, and the distance between the farthest object point and the coordinate origin is 1.8 mm. Thus, according to Eq. (3.19), the required number of samples in the spherical hologram is calculated as 21765(θ)×43530(φ). The angular pitch $\Delta\theta$ and $\Delta\varphi$ are 0.14 mrad, respectively. Figure 3.44 shows amplitude of the generated spherical hologram. In order to improve the computing efficiency, the hologram is separated into several parts and five computers are used to calculate each sub-hologram, and then the completely spherical hologram is synthesized by combining calculated sub-hologram.

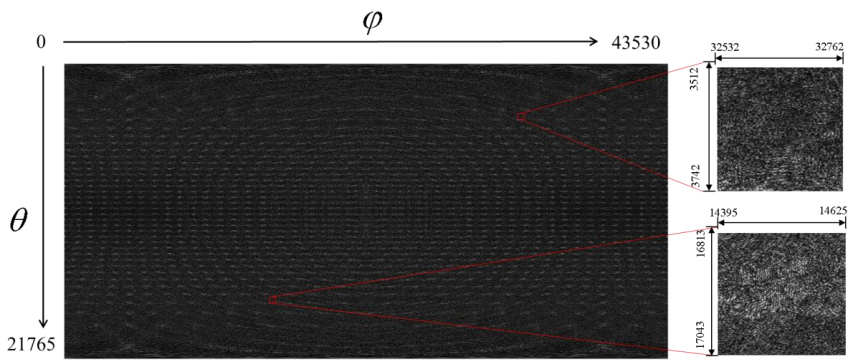

Figure 3.34 Amplitude of the generated spherical hologram.

In order to verify the synthesized hologram, some arbitrary regions of the spherical hologram are selected and reconstructed. Reconstruction process of an interest region is shown in Fig. 3.35. The reconstruction plane ξ-η is set to be normal to the radial line from the coordinate origin to the

center of the selected hologram region. The reconstructed optical field $U(\xi,\eta)$ is given by

$$U(\varepsilon,\eta)=\frac{1}{j\lambda}\sum_{u=1}^{s}\sum_{v=1}^{w}H_r(\theta,\varphi)\frac{\exp(jkd_{u,v})}{d_{u,v}}\cos\Theta, \qquad (3.26)$$

where s and w are the number of the hologram points in the selected region in θ and φ axes, Θ is the angle between normal vector of ξ-η plane and vector pointing from the hologram point $P(\theta,\varphi)$ to reconstruction plane point $P'(\xi,\eta)$ is the distance between the two points.

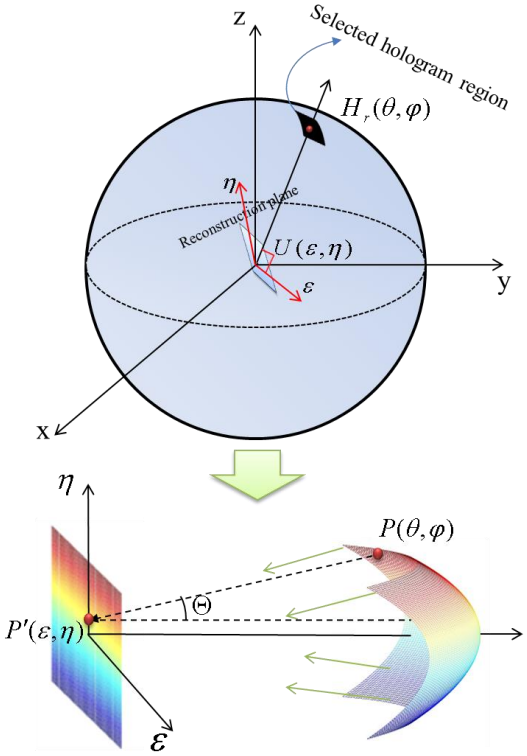

Figure 3.35 Reconstruction process of the selected region.

Figure 3.36 shows the reconstruction results of some partial regions of the spherical hologram, where CR: (θ,φ) is the center region of the selected curved surface. The first column shows the amplitude, phase and their reconstruction images of the selected hologram region with CR: (θ,φ)=(90°,20°), where the hologram size is 230(θ)×230(φ) and size of the reconstruction plane is 300(θ)×300(φ). Furthermore, I arbitrarily select the other regions of the hologram with the same size as the first one, for CR:(110°,110°), CR:(90°,90°), CR:(75°,110°), CR:(70°,270°) and CR:(90°,270°), respectively. The corresponding amplitude, phase and their reconstruction images are also shown in Fig. 3.36.

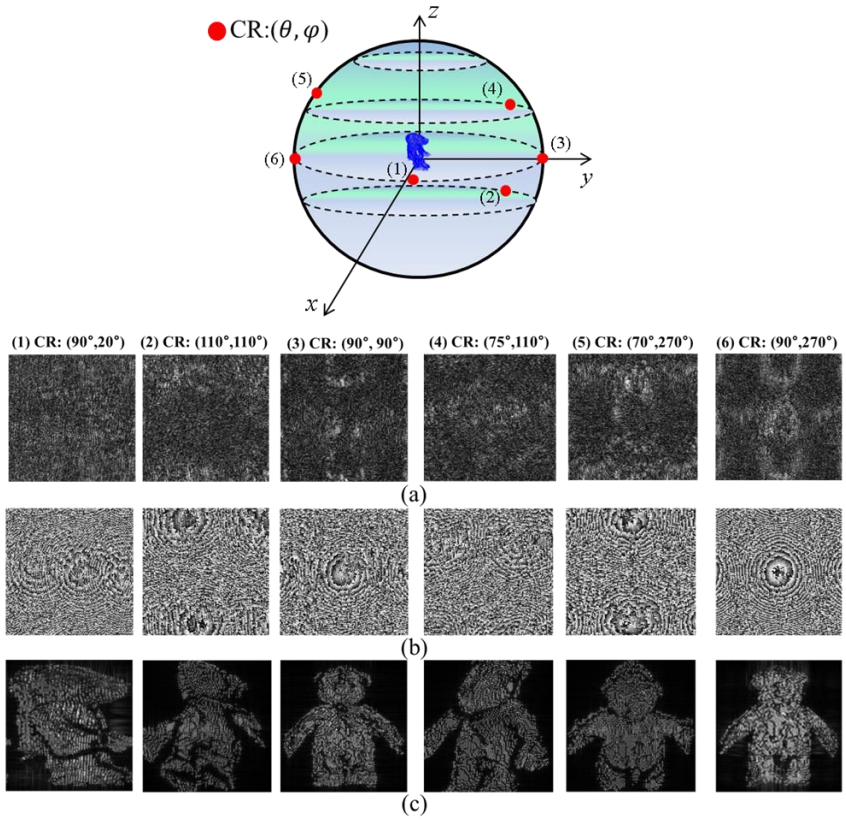

Figure 3.36 Reconstruction of the partial regions of the spherical hologram. (a) Amplitude, (b) phase and (c) reconstruction image of the selected hologram region.

The result demonstrates that the partial region of the spherical hologram synthesized by the proposed method can reconstruct corresponding perspective of the real-existing object successfully. Figure 3.37 shows the effect of HPR process. The same regions of the proposed spherical hologram and the hologram generated without using HPR are selected and reconstructed. In Fig. 3.37 (b), because all the object points are calculated, it is difficult to determine whether the object is looking forwards

or backwards at the viewpoint. Furthermore, Fig. 3.37 (a) show that the spherical hologram generated by the proposed method can clearly portray the shape of the object, whereas it is difficult to identify which region of the object is reconstructed when HPR process is at used as shown in Fig. 3.37 (b). Hence, the identification of visible points is quite an important process for correct occlusion effect in spherical hologram generation.

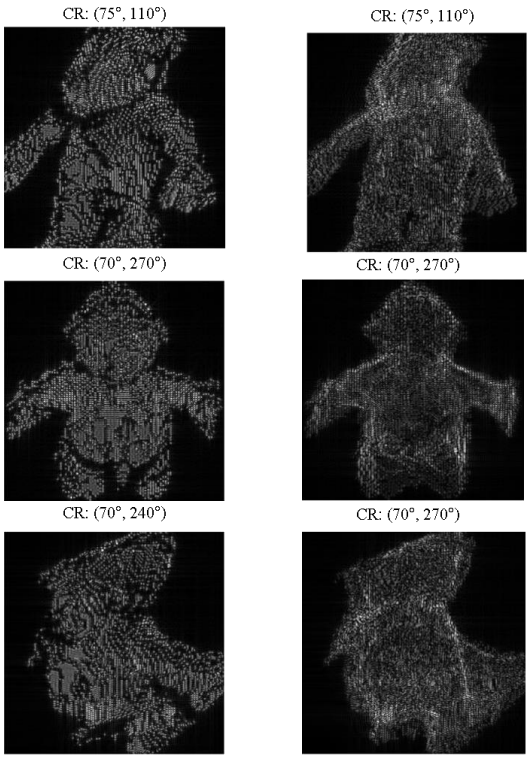

Figure 3.37 (a) Reconstruction image from a partial region of the proposed spherical hologram, (b) reconstruction image from the spherical hologram generated without using the HPR algorithm.

3.5 Summary and discussion

The method that widens FOV by reducing the eyebox size cannot be the ultimate solution for the FOV issue, because eyebox size should be at least larger than 1.3 mm to maintain the accommodation effect. Furthermore, the eyebox size should be determined in accordance with the FOV to support eye rotation within the entire FOV range. Therefore, increasing the SBP is an ideal solution. In this chapter, two SPB enhancement methods are introduced. The first one is temporal multiplexing of high-order diffraction of an SLM. In this method, three HOEs are designed to guide the different diffraction orders to an identical direction with the same intensity. A set of relay lenses and electro-shutters are used to implement the display as if three-SLMs are arranged with seamless effect. As a result, the demonstrated system achieves a three-fold increase in SBP of a single SLM.

A main disadvantage of the first method is the requirement of the mechanical movement in the system. A novel method called *polarization selective holography* is proposed. Unlike the conventional SBP enhancement methods the proposed polarization selective holography does not need to do temporal multiplexing process which requires mechanical movement. It also can get two times increase in terms of SBP without using any additional SLMs. In general, in order to increase the SBP we have to scarify some parameters. In this method, the scarified parameter is contrast i.e. gray level of the SLM. If there is an SLM having larger phase retardation such as 2π~4π we can get more complex distribution of the ACM. However, the more phase variation causes more errors in the amplitude mode holographic

display. Therefore, how to decide an SLM's phase retardation is most important issue in this method.

A curved surface hologram can provide wider field of view. Thus, curved holographic display has a great potential to the near-eye holography. A novel method for generating a spherical hologram of real objects has been proposed in this section. To my best knowledge, it is the first demonstration of 360° spherical hologram of real-existing object. A depth camera is used to extract depth information of the object from different directions. By applying HPR to the spherical hologram synthesis, the occlusion effect can be correctly considered in the proposed method. The experimental results demonstrate that the proposed method is capable of synthesizing a spherical hologram, which contains 360° field of view information of the real-existing 3D objects successfully. We believe that the proposed method is particularly useful in building a database for storing the information of real objects' 360° optical field, so that we can reconstruct any region of the interest.

Chapter 4 Light source selection for near-eye holographic display

4.1 Coherence of light source

Light source plays a critical role in the holographic displays. Laser is a common light source used in the holographic display because of its high temporal and spatial coherence properties. However, the high temporal coherence induces significant speckles in the reconstructed images, which affects the image quality greatly. To alleviate the issue, LED that is a partially coherent light source was attempted as the light source in some reports. However, the low temporal coherence of the LED could constrain the reconstructable depth range of the images. In addition, to get a satisfactory spatial coherency, a spatial filter leads to decrease the illumination energy. In consequence, the coherence properties of the light source directly influence the quality of hologram images on both image sharpness and speckle. This section discusses the fundamental properties of the coherence of the light source and propose a simple alternative for the light source issue of near-eye holography.

4.1.1 Temporal coherence

Temporal coherence measures the correlation between waves observed at different moments in time. When the correlation decreases around 0, the coherence time t_c can be calculated by the phase delay between the two

waves. The coherence length L_c is defined as traveled distance of the wave in t_c. According to the temporal coherence, we can know how monochromatic a light source is. The coherence length of a light source can be obtained based on the Gaussian emission spectrum, and it is given by [86]

$$L_c = \sqrt{\frac{2\ln(2)}{\pi n}} \frac{\lambda^2}{\Delta\lambda} \tag{4.1}$$

where n is the refractive index of the medium, λ is the central wavelength and $\Delta\lambda$ is the full width half maximum of the peak in wavelength spectrum. For measurement of the temporal coherence, we can build a Michelson interferometer or numerically calculate the L_c by substituting the $\Delta\lambda$, which is provided by the laser's manufacturer. Once the fringes are obtained in the Michelson interferometer, when one of the mirrors is translated along the beam path gradually, the time for the beam to travel increases and the fringes become dull and finally are lost, showing temporal coherence.

4.1.2 Spatial coherence

Spatial coherence actually describes how small the size of the light source is. As shown in Fig. 4.1, light from different parts of the light source propagates to a screen thus there is a specific correlation between position A and B. Let us assume that the size of the light source is infinitely small, the optical waves at position A and B have a constant phase delay, which means they have a maximum correlation. In this case, the light source is regarded has a very high spatial coherence.

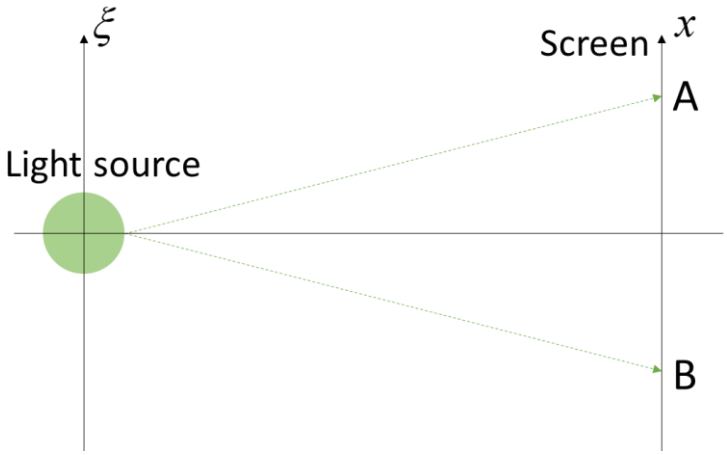

Figure 4.1 Correlation between two light poits from a light source

One way to calculate the degree of spatial coherence is to apply Van Cittert-Zernike theorem. The theorem deal with that the problem of spatial coherence by solving the diffraction problem [90]. In this calculation, an aperture that has the same size with the light source is placed at the position of the light source. The aperture is then illuminated by a spherical wave, which is emerged from a point light source located at position A or B. The optical field on point A of the screen can be found using Fresnel diffraction formula, which is given by

$$U\left(x;x_A\right)=C\times \exp\left[\frac{-jk_0}{2r}\left(x^2\right)\right] \times\int_{\infty}^{\infty}A(\xi)\exp\left\{\frac{jk_0}{r}\left[\left(x-x_A\right)\xi\right]\right\}d\xi \tag{4.2}$$

where C is a constant, optical field of the aperture is determined by $A(\xi)$, and x_A is the coordinate of point A on the screen. Optical field at the point B $U(x;x_B)$ is calculated as the same manner with Eq. (4.2). Finally, the complex

degree of coherence between points A and B is the form of the normalized diffracted field can be calculated as Eq. (4.2) in [86, 90].

$$\gamma_{AB} = \frac{\int_{-\infty}^{\infty} A(\xi) \exp\left\{ \frac{jk_0}{r} \left[(x_A - x_B)\xi \right] \right\} d\xi}{\int_{-\infty}^{\infty} A(\xi) d\xi} = \frac{F\left\{ A(x) \right\}_{k_x = \frac{k_0 (x_A - x_B)}{r}}}{\int_{-\infty}^{\infty} A(\xi) d\xi}. \tag{4.2}$$

4.2 Image sharpness for holographic display

In holographic display, the light source illuminates CGH, which is displayed on an SLM, to reconstruct holographic images. The optical field information on the SLM diffracts incident light wave to reconstruct the desired holographic images. For convenience of explanation, a set of double slits case representing two spatially separated pixels of the SLM, is used for explaining the reconstructed image quality depending on coherence. Fig. 4.2(a) shows how the temporal coherence influence the interference patterns sharpness, and Fig. 4.2(b) shows the spatial coherence case. In Fig. 4.2(a), a light source illuminates the double slits screen with different wavelengths. In double slit plane, two slits function as two individual light sources propagating to the second screen. Note that the optical field at the second plane is calculated by using Fresnel propagation algorithm. The interference pattern formed by the longer wavelength, which is marked in the red line, has a longer period. The superposed result shows that the pattern is imposed by a new envelope curve.

In Fig. 4.2(b), a light source is assumed to have a certain size and two points on the light source are used in the simulation. Same as the first simulation, the two light sources also propagate to the double slits screen and the slits function as the two distinguished light sources to form interference patterns. Since the two point sources have the same wavelength, the interference pattern generated by each point source shifted with a constant phase, thus the superposed interference pattern shows a decreased contrast.

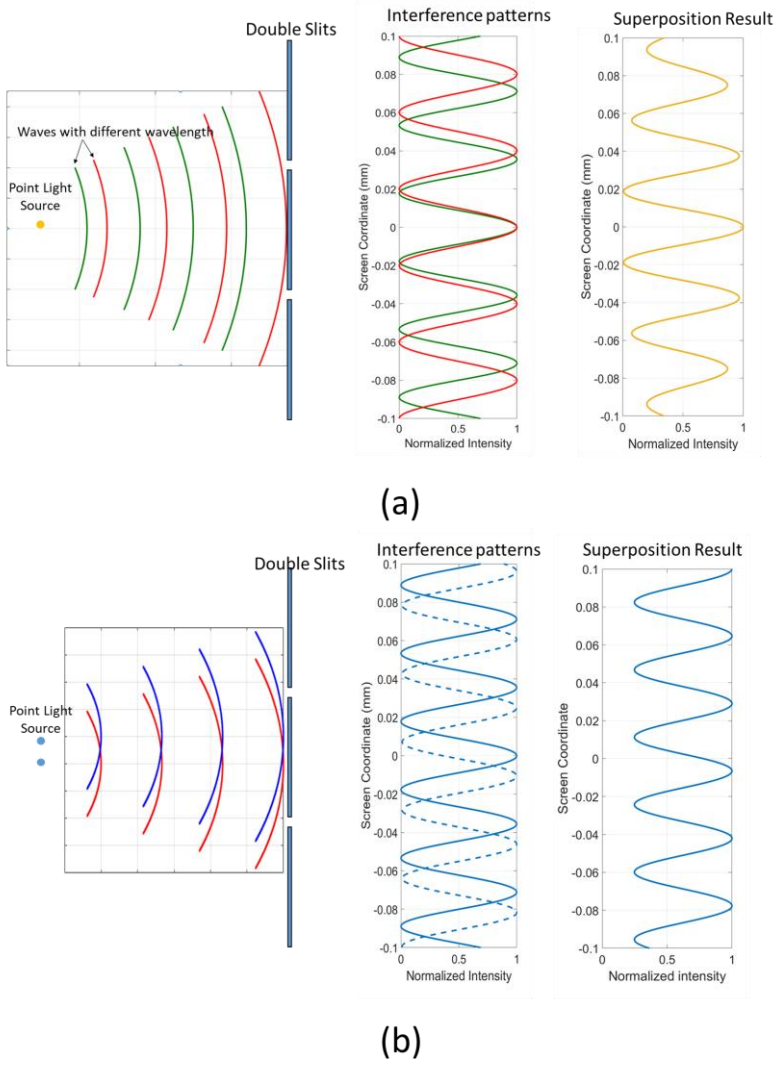

Figure 4.2 Comparison of image sharpness using light sources with different coherencies. (a) How temporal coherence and (b) spatial coherence affect quality of reconstruction images.

The results reveal that the temporal coherence reshapes it by imposing an envelope curve while the spatial coherence directly changes the contrast

of the interference pattern. If we merely take account the above factors, the better coherence properties on both temporal and spatial domain can contribute better reconstruction image qualities. However, another important factor, i.e. speckle, is also a very important, affecting the holographic image. Let us consider a wave emitting from a point source and there is a rough surface on its propagation path. The wave reflected by such a rough surface is the sum of secondary waves from many independent scattering areas. The condition that two secondary waves can interfere is that their light path difference should be shorter than the coherent length, while the coherent length is directly associated with the temporal coherence.

A simple experiment, which illuminates the same hologram with LD and an LED, is carried out to compare the reconstruction images. Figure 4.3(a) shows a hologram reconstructed at several different depths by LD and LED, respectively and Fig. 4.3(b) shows the light bandwidths of the light sources used in the experiment. Note that, a spatial filter composed of a micro pinhole and an objective lens is used for the two light sources so that the experiments are carried out under the same spatial coherence. Since, the temporal coherence length of the LD is much longer than LED, it can reconstruct quite a sharp image at a long depth range while the high temporal coherence leads to the severe speckle noises. On the other hand, the LED based holographic images show very low speckle noise level, but the expressible depth range is limited.

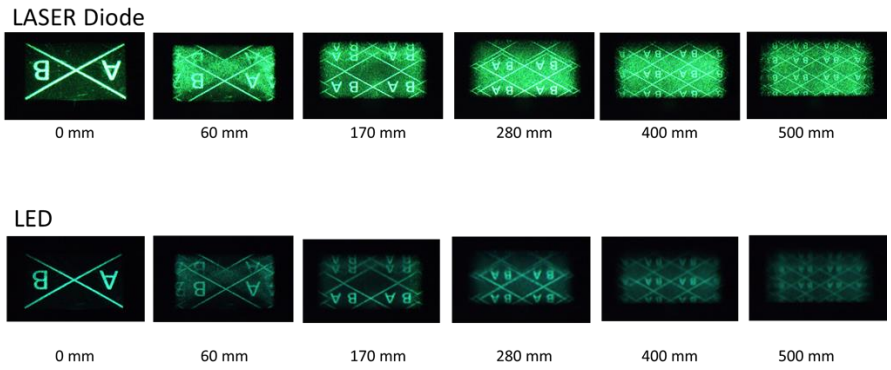

(a)

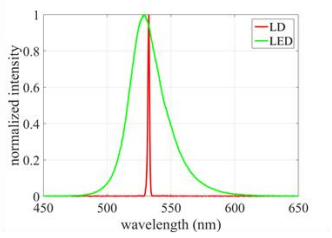

(b)

Figure 4.3 (a) Holograms reconstructed at different depths from an SLM using LD and LED light source. (b) Spectrum of the light source.

4.3 Ideal optical design for LED based near-eye holography

Table 4.1 Features of the two light sources (same spatial coherence) for holographic display.

Light source	Temporal coherence	Speckle noise	Expressible depth range	Image sharpness
LD	High	Server	Long	High
LED	Low	Weak	Short	$\propto$ Depth

Table 4.1 shows the features of the two light sources for holographic display, when the two light sources are filtered by the same spatial filter. The inherence properties of light source determine the temporal coherence which is unable to adjust. It means the speckle noise cannot be removed without adding optical or mechanical systems. Therefore, the solution proposed in this section focuses on the adjustable factor, i.e. expressible depth range, which also determines the image sharpness of LED. Figure 4.4 shows the schematic diagram of the proposed method. A fiber coupled or a spatial filtered LED light source is used as the light source to suppress the speckle noise. As shown in Table 4.1, the expressible depth range maintaining the sharpness of holographic image is limited in a short range [87-89]. I use a short focal length, which is shorter than the expressible depth range, and place the SLM at the focal plane of the eyepiece. In the configuration, the SLM can reconstruct the hologram from infinity to the nearest visible depth

of user by merely reconstructing the image in a short depth range S according to the equation

$$S = f - \frac{1}{D_{near} + D_f}, \tag{4.3}$$

where f is the focal length of the eyepiece and its dioptric notation is D_f. And D_{near} is diopter of the nearest visible distance, which is generally defined as 5 diopter. In the method, the expressible depth range of LED based holography is defined as 0.17 diopter, thus the power of the eyepiece should be shorter than 0.17 diopter. To reconstruct the image from infinity to the nearest visible depth while maintain image sharpness, the reconstruction depth range S just need to cover from 0 to 14 mm. As shown in Fig. 4.3 (a) LED based holography is sufficiently able to reconstruct a good quality image in this range.

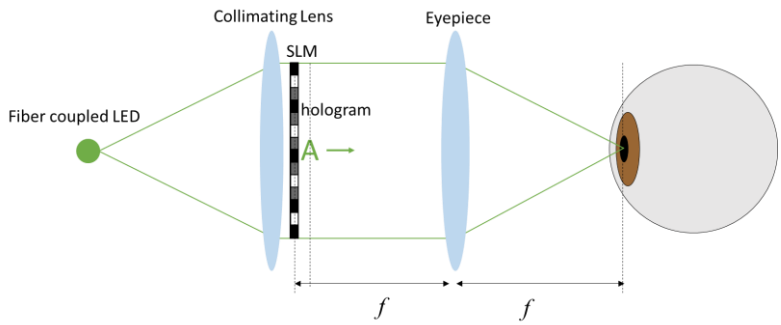

Figure 4.4 Optical design for the near-eye holography using a light source with low temporal coherence.

Figure 4.5 shows the experimental results using the proposed method. The object letters A and B are constructed from 0 to 5 diopter by reconstructing the hologram from 0 to 14 mm from the SLM. The result reveals that the proposed LED based holography can have quite a good image quality for a sufficiently long depth range. The noise-like background is the DC term, which can be removed using single side band holography technic. The purpose of the experiment is to show that only using an LED can also cover the complete depth range for user. As a result, the proposed method can effectively suppress the speckle noise for near-eye holographic display.

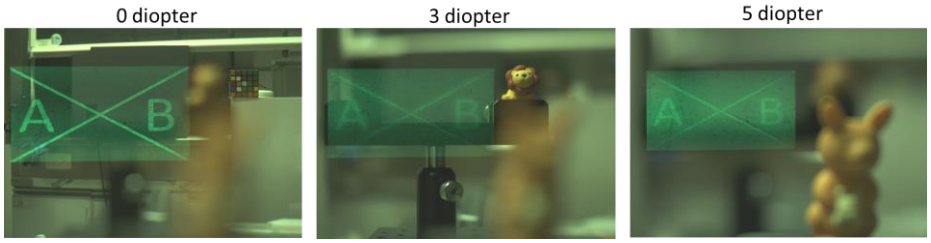

Figure 4.5 Reconstructed hologram at different depth plane using the proposed optical configuration.

4.4 Summary and discussion

In summary, a light source with high spatial coherence and moderate temporal coherence can provide a high quality images with good sharpness and minimum speckle noise in holographic display. To use a low temporal coherence light source such as LED, a magnification optical system should be used to mitigate the short expressible depth rage. The experimental results shows that even if an LED is used as the light source, the holographic display can also reconstruct the image from infinity to nearest focal plane of observers. If a light source has the ability that changes the temporal coherence property, it would be an ideal light source for the near-eye holographic display.

Chapter 5 Conclusion

AR/VR near-eye displays provide a lot of potential to create new life style for people. To develop an ideal near-eye devices several issues should be ultimately solved, which are mentioned in the introduction section. Compared with the other 3D display techniques, holography is the best way to create natural focus cues. However, the holography technique has not yet reached a mature step to make consumers widely accept it. This dissertation has proposed several approaches to solve the fundamental problems of the near-eye holography. The issues involves form factor reduction, FOV expansion, and light source selection.

To reduce the form factor of the conventional holographic display, I used a multifunctional HOE: MLHOE to replace the beam splitter and the eyepiece lens of the display system. In this study, the optical characteristics of the HOE are analyzed based on coupled-wave theory. The analysis mainly targets on the angular selectivity, angular deviation under Bragg-mismatched condition, and diffraction efficiency uniformity of the HOE. Considering all of the evidences, I conclude that the HOE can be a very good optical element for a near-eye holographic display.

For the next issue: FOV, I discussed the topic from the tradeoff between FOV and eyebox size. The method of reducing the eyebox size to enlarge the FOV, cannot be the ultimate solution because the accommodation effect occurs when the eyebox size is larger than a certain criterion. Thus, two SBP enhancement methods are proposed. The first method uses three different

diffraction orders of an SLM to get a three-fold increase in SBP. However, the requirement of mechanical movement causes the large form factor of the system. Thus, another SBP enhancement method without any mechanical movements named *polarization selective holography* is proposed. In the method, an SLM generates two different signals with two different modulation modes. The different modulation modes are realized by using a wave retarder and a polarizer with different variables. Therefore, by placing the stationary optical elements at the paths of two different diffraction order of an SLM, the SLM can indecently modulate the two different holograms. As a result, I can increase the SBP two times for a single SLM.

Speckle noise issue is also discussed in this dissertation. Use of LED can suppress the speckle noise in the holographic display. Using the LED, however, cannot reconstruct images located far from the SLM. Thus, a magnification optical system should be used to mitigate the short expressible depth range. If a light source has the ability that can change the temporal coherence property, it would be an ideal light source for the near-eye holographic display.

Although the holographic display still has many problems to be solved, I believe it has chances to succeed in the near-eye display area especially for AR.

Bibliography

1. R. T. Azuma, “A survey of augmented reality. Presence: *Teleoperators and virtual environments*,” 6, **4**, 335-385(1997).
2. J. sardegna, S. Shelly, A. R. Rutzen, and S. M. Steidl, “The encyclopedia of blindness and vision impairment 2nd edition,” Infobase Publishing. P. 253. ISBN 978-0-8160-6623-0. Retrieved 30 (2014)
3. A. Cameron, “The application of holographic optical waveguide technology to the Q-Sight™ family of helmet-mounted displays,” Proc. SPIE, **7326** (2009).
4. D. Roberts, “Soldier-worn augmented reality system for tactical icon visualization,” Proc. SPIE, 8383 (2012).
5. A. Cameron, “Optical waveguide technology & its application in head mounted displays,” Proc. SPIE **8383** (2012).
6. J.-A. Piao, G. Li, M.-L. Piao, and N. Kim, “Full color holographic optical element fabrication for waveguide-type head mounted display using photopolymer,” J. Opt. Soc. Korea **17,** 242-248 (2013).
7. M. G. Tomilin, “Head-mounted displays,” J. Opt. Technol. **66**, 528-533 (1999).
8. W. T. Welford, “Aberrations of optical systems” Higer, Bristol, UK(1986).
9. J. Liang and D. R. Williams, “Aberrations and retinal image quality of the normal human eye,” J. Opt. Soc. Am. A **14**, 2873-2883 (1997).
10. J. C. Wyant, and K. Creath, “Basic wavefront aberration theory for

optical metrology," in Applied Optics and Optical Engineering, R. R. Shannon, J. C. Wyant, eds. (Academic, New York), Vol. XI (1992).

11. B. Kress and T. Starner, "A review of head-mounted displays (HMD) technologies and applications for consumer electronics" Proc. SPIE, 8720 (2013).
12. B. Lee, "Three-dimensional displays, past and present," Phys. Today **66**(4), 36-41 (2013).
13. M. Lambooij and W. Ijsselsteijn, "Visiual discomfort and visual fatigue of stereoscopic displays," Journal of Imaging Science and Technology **53**, 0302011-030214(2009).
14. D. M. Hoffman and M. S. Banks, "Focus information is used to interpret binocular images," J. Vision, **13**, 1-17(2010).
15. S. J. Watt, K. Akeley, M. O. Ernst, and M. S. Banks, "Focus cues affect perceived depth," J. Vision **5**, 834-862(2005).
16. Wann, J.P., S. Rushton, and M. M. Williams, "Natural problems for stereoscopic depth perception in virtual enviroments," Vision Res., **35**, 2731-2736(1995).
17. T. Shibata, J. Kim, D. M. Hoffman, and M. S. Banks, "The zone of comfort: Predicting visual discomfort with stereo displays," J. Vision **11**, 1-29(2011).
18. S. Liu, H. Hua, and D. Cheng, "An optical see-through head-mounted display with addressable focus cues," *in IEEE Transactions on Visualization and Computer Graphics,* (2010).
19. S. Liu, D. Cheng, and H. Hua, "An optical see-through head-mounted display with addressable focal planes," *Proceedings of 2008 IEEE and*

ACM International Symposium on Mixed and Augmented Reality (ISMAR 2008), 33-42(2008).

20. S. Shiwa, K. Omura, and F. Kishino, "Proposal for a 3-D display with accommodative compensation: 3DDAC," J. SID, **4** 255-261(1996).
21. E. F. Eves, "Parallax stereogram and process of making same," U.S. Patent 725,567(1903).
22. H. J. Lee, H. Nam, J. D. Lee, H. W. Jang, M. S. Song, B. S. Kim, J. S. Gu, C. Y. Park, and K. H. Choi, "A high resolution autostereoscopic display employing a time division parallax barrier," in *SID international symposium Digest of Technical Papers* (Society for Information Display) **37**, 81-84(2006).
23. G. Hamagishi, "Analysis and improvement of viewing conditions for two-view and multi-view 3D displays," in *SID International symposium Digest of Technical Papers* (Society for information Display), **40**, 340-343(2009).
24. G. Lippman, "La photographie integrale," C. R. Acad. Sci. **146**, 446-451 (1908).
25. F. Okano, H. Hoshino, J. Arai, and I. Yuyama, "Real-time pickup method for a three-dimensional image based on integral photography," Appl. Opt. **36**, 1598-1603 (1997).
26. B. Lee, J.-H. Park, and S.-W. Min, "Three-dimensional display and information processing based on integral imaging," in *Digital Holography and Three-Dimensional Display* T.-C. Poon, ed. (Springer, 2006), Chapt. 12, 333-378.
27. J.-H. Park, K. Hong, and B. Lee, "Recent progress in three-dimensional

information processing based on integral imaging," Appl. Opt. **48**, H77-H94 (2009).

28. G. Li, K.-C. Kwon, G.-H. Shin, J.-S. Jeong, K.-H. Yoo, and N. Kim, "Simplified integral imaging picup method for real object using a depth camera," J. Opt. Soc. Korea, **16**, 381-385(2012).
29. D. Lanman, M. Hirsch, Y. Kim, and R. Raskar, "Content-adaptive parallax barriers: optimizing dual-layer 3d displays using low-rank light field factorization." *ACM Trans. Graph.* (SIGGRAPH Asia) 29, 163:1-163:10 (2010).
30. D. Lanman, G. Wetzstain, M. Hirsch, W. Heidrich, and R. Raskar, "Polarization fields: Dynamic light field display using multi-layer lcds." *ACM Trans. Graph.* (*SIGGRAPH Asia*) **30**,186 (2011).
31. G. Wetzstein, D. Lanman, W. Heidrich, and R. Raskar, "Layerd 3D: Tomographic image synthesis for attenuation-based light field and high dynamic range displays" *ACM Trans. Graph.* (*SIGGRAPH*) **30**, 1-11.
32. S. Lee, C. Jang, S. Moon, J. Cho, and B. Lee, "Additive light field displays: realization of augmented reality with holographic optical elements," *ACM Trans. On Graphics*, (*SIGGRAPH*) **35**, article 60 (2006).
33. D. Lanman and D. Luebke, "Near-eye light field displays." *ACM Trans. Graph.* (*SIGGRAPH Asia*) **32**, 220:1-220:10 (2013).
34. M. Zwicker, W. Matusk, F. Durand, and H. Pfister, "Antialiasing for automultiscopic 3D displays," In EGSR (2006).
35. Y. Kim, E. Stoykova, H. Kang, S. Hong, J. Park, J. Park, and J. Hong, "Seamless full color holographic printing method based on spatial partitioning of SLM," Opt. Express 23(1), 172-182 (2015).

36. N. Fukaya, K. Maeno, O. Nishikawa, and K. Matsumoto, “Expansion of the image size and viewing zone in holographic display using liquid crystals devices,” Proc. SPIE 2406, 283-289 (1995).
37. K. Maeno, N. Fukaya, and O. Nishikawa, “Electro-holographic display using 15Mega pixels LCD,” Proc. SPIE 2652, 15-23 (1995).
38. T. Kozacki, M. Kujawinska, G. Finke, B. Kennelly, and N. Pandey, “Extended viewing angle holographic display system with tilted SLMs in a circular configuration,” Appl. Opt. 51(11), 1771-1780 (2012).
39. J. Hahn, H. Kim, Y. Lim, G. Park, and B. Lee, “Wide viewing angle dynamic holographic stereogram with a curved array of spatial light modulators,” Opt. Express 16(16), 12372-12386 (2008).
40. F. Yaras, H. Kang, and L. Onural, “Circular holographic video display system,” Opt. Express 19(10), 9147-9156 (2011).
41. T. Kozacki, G. Finke, P. Garbat, W. Zaperty, and M. Kujawinska, “Wide angle holographic display system with spatiotemporal multiplexing,” Opt. Express 20(25), 27473-27481 (2012).
42. H. Sasaki, K. Yamamoto, Y. Ichihashi, and T. Senoh, “Image size scalable full-parallax coloured three-dimensional video by electronic holography,” Sci. Rep. 4, 4000 (2014).
43. H. Sasaki, K. Yamamoto, K. Wakunami, Y. Ichihashi, R. Oi, and T. Senoh, “Large size three-dimensional video by electronic holography using multiple spatial light modulators,” Sci. Rep. 4, 6177 (2014).
44. T. Mishina, M. Okui, and F. Okano, “Viewing-zone enlargement method for sampled hologram that uses high-order diffraction,” Appl. Opt. 41(8), 1489-1499 (2002).

45. G. Li, J. Jeong, D. Lee, J. Yeom, C. Jang, S. Lee, and B. Lee, "Space bandwidth product enhancement of holographic display using high-order diffraction guided by holographic optical element," Opt. Express, **23**, 33170-33183 (2015).
46. G. Li, D. Lee, Y. Jeong, J. Cho, and B. Lee, "Holographic display for see-through augmented reality using mirror-lens holographic optical element," Opt. Lett., **41** 2486-2489 (2016).
47. G. Li, J. Jeong, J. Yeom, and B. Lee "Fourier holographic display for augmented reality using holographic optical element", *Proc. SPIE 9770, Advances in Display Technologies VI: 3D, Holographic, and HM displays*, 9770-12 (2016).
48. G. Li A.-H, Phan, N. Kim, and J.-H. Park, "Synthesis of computer-generated spherical hologram of real object with 360 degree field of view using a depth camera," Appl. Opt., **52**, 3567-3575 (2013).
49. S. Katz, A. Tal, and R. Basri, "Direct visibility of point sets," ACM Trans. Graph. **26**, 2-11, (2007).
50. A. Maimone, A. Georgiou, and J. Kollin, "Holographic near-eye displays for virtual and augmented reality," *ACM Trans. Graphics*, **36**, Article 85, (2017).
51. R. R. A. Syms, Practical Volume Holography (Cambridge University Press, 2002).
52. J. W. Goodman, *Introduction to Fourier Optics*, 4th ed. Freeman, 2017.
53. P. Yeh, *Introduction to Photorefractive Nonlinear Optics*, Wiley and Sons, New York (1993).
54. H. Kogelnik, "Coupled wave theory for thick hologram gratings," Bell

Syst. Tech. J. 48. 2909-2947 (1969).

55. P. Hariharan, “Holographic recording materials: Recent developments,” Opt. Eng. 19, 636 (1980)

56. M.-L. Piao and N. Kim, “Achieving high levels of color uniformity and optical efficiency for a wedge-shaped waveguide head mounted display using a photopolymer,” Appl. Opt. 53(10), 2180-2186 (2014).

57. H. Berneth, F.-K. Bruder, T. Facke, R. Hagen, D. Honel, D. Jurbergs, T. Rolle, and M.-S. Weiser, “Holographic recording aspects of high-resolution Bayfol HX photopolymer,” Proc. SPIE 7957, 79570H (2011).

58. N. Kim and E. S. Hwang, “Analysis of optical properties with photopolymers for holographic application,” J. Opt. Soc. Korea 10, 1-10 (2006).

59. K. Hong, J. Yeom, C. Jang, J. Hong, and B. Lee, “Full-color lens-array holographic optical element for three-dimensional optical see-through augmented reality,” Opt. Lett. 39, 127–130 (2014).

60. K. Hong, J. Yeom, C. Jang, G. Li, J. Hong, and B. Lee, “Two-dimensional and three-dimensional transparent screens based on lens-array holographic optical elements,” Opt. Express 22, 14363-14374 (2014).

61. R. R. A. Syms and L. Solymar, “Localized one-dimensional theory for volume holograms,” Opt. Quantum Electron. 13, 415-419 (1981).

62. Y. Luo, J. Castro, J. K. Barton, R. K. Kostuk, and G. Barbastathis, “Simulations and experiments of periodic and multiplexed gratings in volume holographic imaging systems,” Opt. Express 18, 19273-19285 (2010).

63. C. Jang, C.-K. Lee, J. Jeong, G. Li, S. Lee, J. Yeom, K. Hong, and B. Lee,

"Recent progress in see-through three-dimensional displays using holographic optical elements," Appl. Optics, vol. 55, A71-A85 (2016).

64. J. Yeom, J. Jeong, C. Jang, G. Li, K. Hong, and B. Lee, "Three-dimensional/two-dimensional convertible projection screen using see-through integral imaging based on holographic optical element," Applied Optics, vol. 54, 8856-8862 (2015).
65. O. Bryngdahl and A. Lohmann, "Single-sideband holography," J. Opt. Soc. Am. **58**, 620-624 (1968).
66. Y. Takaki, and Y. Tanemoto, "Band-limited zone plates for single-sideband holography," Appl. Opt. **48**, H64-H70 (2009).
67. H. Kim, C.-Y. Hwang, K.-S. Kim, J. Roh, W. Moon, S. Kim, B.-R. Lee, S. Oh, and J. Hahn, "Anamorphic optical transformation of an amplitude spatial light modulator to a complex spatial light modulator with square pixels," Appl. **53**, G139-G146 (2014).
68. K. Matsushima, H. Schimmel, and F. Wyrowski, "Fast calculation method for optical diffraction on tilted planes by use of the angular spectrum of plane waves," J. Opt. Soc. Am. A **20**, 1755-1762 (2003).
69. K. Matsushima, "Computer-generated holograms for three-dimensional surface objects with shade and texture," Appl. Opt. **44**, 4607-4614(2005).
70. H. Kim, J. Hahn, and B. lee, "Mathematical modeling of triangle-mesh-modeled three-dimensional surface objects for digital holography," Appl. Opt. **47**, D117-D127 (2008).
71. M. Born and E. Wolf, "Principles of Optics" (Pergamon, Oxford, 1975), 464-473.
72. R. J. Noll, "Zernike polynomials and atmospheric turbulence," J. Opt.

Soc. Am. 66, 207 (1976).

73. H. Kim, J. Hahn, and B. Lee, “Mathematical modeling of triangle-mesh-modeled three-dimensional surface objects for digital holography,” Appl. Opt. **47**, D117-D127 (2008).

74. J. W. Goodman and R. W. Lawrence, “Digital image formation from electronically detected holograms,” Appl. Phys. Lett. 11, 77-79 (1967).

75. E. N. Leith and J. Upatnieks, “Reconstructed wavefronts and communication theory,” J. Opt. Soc. Am. 52, 1123-1130 (1962).

76. B. Kemper and G. von Bally, “Digital holographic microscopy for live cell applications and technical inspection,” Appl. Opt. 47, A52–A61.

77. G. Westheimer, “Pupil size and visual resolution,” Vision Res. **4**, 39-45 (1964).

78. S. Marcos, E. Moreno, and F. Navarro, “The depth-of-field of the human eye from objective and subjective measurements,” Vision Research **39**, 2039-2049 (1999).

79. N. Lopez-Gil, I. Iglesias, and P. Artal, “Retinal image quality in the human eye as a function of the accommodation,” Vision Research **38**, 2897-2907 (1998).

80. G. Westheimer, “The Maxwellian view,” Vision Research **6**, 669-682 (1966).

81. X. Yi, and P. Yeh, “Effect of grating detuning in holographic storage,” Vol. 4, *CLEO/Pacific Rim 99,* 1175-1176, IEEE Press (1999).

82. M.-L. Hsieh and K. Y. Hsu, “Grating detuning effect on holographic memory in photopolymers,” Opt. Eng. **40** 2125-2133 (2001).

83. J. R. Clark, “A new calculus for the treatment of optical system, I.

Description and Discussion of the Calculus," J. Opt. Soc. Am. **31**, 488-493(1941).

84. J. Hahn, H. Kim, S.-W, Cho, and B. Lee, "Phase-shifting interferometry with genetic algorithm-based twin image noise elimination," Applied Optics, **47**, 4068-4076 (2008).
85. J. Hahn, H. Kim, and B. Lee, "Optimization of the spatial light modulation with twisted nematic liquid crystals by a genetic algorithm," Appl. Opt. **47**, 2357 (2008).
86. B. E. A. Saleh and M. C. Teich, "Fundamentals of Photonics", Canada, Wiley Interscience, 1991.
87. T. Kozacki and M. Chlipala, "Color Holographic display with white light LED source and single phase only SLM," Opt. Express **24**, 2189-2199 (2016).
88. M. Oikawa, T. Shimobaba, T. Yoda, H. Nakayama, A. Shiraki, N. Masuda, and T. Ito, "Time-division color electroholography using one-chip RGB LED and synchronizing controller," Opt. Express **19**, 12008-12013 (2011).
89. E. Moon, M. Kim, J. Roh, H. Kim, and J. Hahn, "Holographic head-mounted display with RGB light emitting diode light source," Opt. Express **22**, 6526-6534 (2014).
90. F. Zernike, "The concept of degree of coherence and its application to optical problems," Physica. 5: 785-795 (1938)

Appendix

Portions of the work discussed in this dissertation are also presented in the following publications:

[Chapter 2.3] G. Li, D. Lee, Y. Jeong, J. Cho, and B. Lee, “Holographic display for see-through augmented reality using mirror-lens holographic optical element,” Optics Letters, vol. 41, no. 26, pp. 2486-2489, 2016

[Chapter 3.2] G. Li, J. Jeong, D. Lee, J. Yeom, C. Jang, S. Lee, and B. Lee, “Space bandwidth product enhancement of holographic display using high-order diffraction guided by holographic optical element,” Optics Express, vol. 23, no. 26, pp. 33170-33183, 2015.

[Chapter 5.3] G. Li, A.-H, Phan, N. Kim, and J.-H. Park, “Synthesis of computer-generated spherical hologram of real object with 360 degree field of view using a depth camera,” Applied Optics, vol. 52, 3567-3575, 2013.

[Chapter 5.3.3] G. Li, K. Hong, J. Yeom, N. Chen, J.-H. Park, H. Kim, “Acceleration method for computer generated spherical hologram calculation of real objects using graphics processing unit,” Chin. Opt. Lett., vol. 12, article 060016, 2014